Diverse late Neoarchean magmatism in northeastern North China Craton: consequences of crustal growth, recycling, and magma mixing

Hongxiang Zhang[a], Richard M. Palin[b], Jin Liu[a, c]*, Jian Zhang[d], Changquan Cheng[e], Zhenghong Liu[a, c], Chen Zhao[f], Chao Zhang[f]

[a] *College of Earth Sciences, Jilin University, 2199 Jianshe Street, Changchun, 130061, China*

[b] *Department of Earth Sciences, University of Oxford, South Parks Road, Oxford, OX1 3AN United Kingdom*

[c] *Key Laboratory of Mineral Resources Evaluation in Northeast Asia, Ministry of Natural Resources, Changchun 130061, China*

[d] *Department of Earth Sciences, The University of Hong Kong, Pokfulam Road, Hong Kong, China*

[e] *School of Earth Sciences and Engineering, Sun Yat-sen University, Zhuhai 519000, China*

[f] *Shenyang Center of Geological Survey, China Geological Survey, Shenyang, Liaoning, China*

Corresponding author: Jin Liu

*E-mail: **liujin@jlu.edu.cn**

Abstract

The North China Craton (NCC) preserves a wide range of Neoarchean magmatic rocks, which provide valuable insights into the origins of magmatic diversity and associated tectonic processes that occurred on the early Earth. Here, we examine three lithologies from the southern Jilin terrane, a major component of the NCC: potassic granites, sanukitoids (granodiorite and diorite), and mafic enclaves (amphibolite and hornblendite). Zircon U–Pb geochronology confirms that these units crystallized around 2510 Ma. The potassic granites exhibit typical geochemical characteristics of crust-derived rocks, indicating that their magma source was related to partial melting of early-formed TTG rocks within a thickened lower crust. Whole-rock geochemistry, Nd isotopes, and zircon Hf isotope data reveal that the amphibolite enclaves formed from mafic magmas derived from partial melting of an enriched lithospheric mantle. In contrast, the hornblendite enclaves are interpreted as altered cumulates that formed through low-pressure (0.6–1.0 GPa) fractionation of 25–45 vol. % clinopyroxene and olivine from the amphibolite parental magmas. The sanukitoids contain abundant mafic microgranular enclaves and exhibit disequilibrium textures. These characteristics, together with hybrid geochemical signatures, suggest a magma mixing origin. Geochemical modelling further indicates that the granodiorite and diorite resulted from mixing 70–50 vol. % syenogranite with 30–50 vol. % amphibolite. These findings, together with previous studies, provide evidence for a Neoarchean subduction-collision-dominated geodynamic mechanism leading to the evolution of continental crust in the northeastern NCC, with localized contributions from mantle plumes.

Keywords: North China Craton; Neoarchean magmatism; magma mixing; fractional crystallization; sanukitoid; geodynamic regime

1 Introduction

The origin of Earth's early continental crust, the dominant tectonic regime during its formation, and the processes responsible for subsequent cratonic stabilization and maturation are central questions in Precambrian geology (Zhai et al., 2020). The late Archean represents a critical period for the evolution and maturation of continental crust, being marked by the widespread occurrence of diverse magmatic suites (Laurent et al., 2014). During this period, magmatism followed a distinct evolutionary trend from tonalite-trondhjemite-granodiorite (TTG) granitoids towards calc-alkaline compositions (Cawood et al., 2022; Laurent et al., 2014). This transition culminated in the extensive emplacement of potassic granitoids and sanukitoid magmas, which are widely recognized as key markers of cratonic maturation (Cawood et al., 2022). However, several fundamental aspects of this transition remain debated.

One unresolved issue is the variability in the timing of cratonization across different regions. While many cratons, such as the Kaapvaal and Superior, achieved cratonization by the early Neoarchean (~2.7 Ga), others—including the North China and Dharwar Cratons—record prolonged tectonothermal activity extending into the late Neoarchean (Cawood et al., 2022; Dey et al., 2016; Dey and Moyen, 2020; Sun et al., 2024; Zhao and Cawood, 2012). This spatiotemporal discrepancy raises a fundamental question: do these late-stage events represent localized tectonic responses, or are they manifestations of a broader, global geodynamic process? A second unresolved issue concerns the mechanisms that drive cratonic maturation. Proposed models include subduction-related plate tectonics (Moyen, 2019), lithospheric dripping or delamination (Nebel et al., 2018), and mantle plume activity (Fischer and Gerya, 2016; Lin and Beakhouse, 2013). Despite extensive study, a unified explanation that accounts for the diversity of magmatic processes observed during craton evolution is still lacking. Therefore, detailed investigation of the Neoarchean rock record, particularly in cratons like the North China Craton (NCC), is essential for resolving these outstanding questions.

The southern Jilin terrane, an important segment of the NCC, preserves a diverse suite of Neoarchean igneous rocks, including TTG, potassic granite, quartz diorite, and meta-volcanic rocks (Li et al., 2023). This well-preserved record provides a valuable opportunity to explore the processes of crustal evolution, cratonic maturation, and the origins of magmatic diversity during the Neoarchean. In this study, we focus on a series of potassic granites, granodiorites, quartz diorites, and associated mafic enclaves from the southern Jilin terrane. We present new zircon U–Pb geochronology and Lu–Hf isotopic data, along with whole-rock geochemistry and Sm–Nd isotopes. By integrating these datasets with rhyolite-MELTS modelling, we reveal that they experienced a complex petrogenetic evolution involving partial melting, fractional crystallization, and magma mixing. Geochemical evidence supports a subduction-related origin for this magmatism, reinforcing the hypothesis that late Neoarchean magmatic activity in the

NCC was linked to subduction and microcontinental collision. When viewed within a broader geodynamic context, these results provide new constraints on models of Neoarchean cratonization and offer important insights into the processes that shaped the early continental crust at a global scale.

2 Geological background

The NCC is generally considered an amalgamation of multiple Archean micro-blocks, although its detailed tectonic subdivisions remain debated. One perspective suggests that the craton can be further subdivided into several micro-blocks (**Fig. 1a**), which merged by the end of the Neoarchean to form a coherent craton (Zhai, 2011, 2014). In contrast, other researchers propose that the Eastern and Western Blocks did not join together until either 2.5 Ga (Huang et al., 2020; Kusky et al., 2016) or 1.85 Ga (Zhao and Cawood, 2012; Zhao et al., 2012), marking a late establishment of the NCC (**Fig. 1b**). The Eastern Block can be further subdivided into the Longgang Block and Nangrim Block, which collided at 1.9–1.85 Ga along the Jiao–Liao–Ji belt (Zhao et al., 2012). The Eastern Block witnessed multiple magmatic episodes between 3.8 and 2.5 Ga (Wan et al., 2023). Among these events, late Neoarchean magmatism was the most widespread, producing extensive TTG and greenstone belts throughout the NCC.

The southern Jilin terrane, situated in the northeastern Longgang Block, is a well-preserved Neoarchean geological unit within the NCC. This terrane experienced two main magmatic events at ~2.7 Ga and 2.6–2.5 Ga. The 2.6–2.5 Ga event marks the peak of Neoarchean magmatic activity in the southern Jilin terrane (Guo et al., 2015, 2016, 2017, 2018 ; Li et al., 2023). Neoarchean lithological assemblages are extensively exposed in the Tonghua-Jiapigou-Helong areas, which are bounded to the northwest by the Xingmeng Orogenic Belt and to the southeast by the Paleoproterozoic Jiao–Liao–Ji belt (Li et al., 1996; Shen et al., 1994; Wu et al., 1997). The main lithologies in this terrane include TTG, metamorphic supracrustal rocks, and minor occurrences of potassic granite and diorite (**Fig. 1c**) (Guo et al., 2015; Li et al., 2023). The Neoarchean supracrustal and TTG rocks underwent regional metamorphism around 2.5 Ga and record counterclockwise *P*–*T*–*t* paths (Ge et al., 2003). Sporadic potassic granites and quartz diorites share emplacement ages roughly contemporaneous with regional metamorphism (Shan et al., 2022). Based on the degree of metamorphism, the crystalline basement of the southern Jilin terrane can be divided into high-grade terranes and greenstone-granite belts. The high-grade terranes have undergone amphibolite- to granulite-facies metamorphism, while the greenstone-granite belts experienced greenschist- to amphibolite-facies metamorphism (Li et al., 1998; Shen et al., 1994).

The supracrustal rocks in the southern Jilin terrane mainly consist of amphibolites, pelitic gneisses, quartzites, and banded iron formations (BIF) (Guo et al., 2015, 2016; Li et al., 1998; Shen et al., 1994). Geochronological data indicate that these rocks formed during two periods: 2.68–2.65 Ga and 2.59–2.53 Ga. The 2.68–2.65 Ga supracrustal rocks are primarily distributed in the Helong granite-greenstone belt, with a few ~2.68 Ga felsic supracrustal rocks reported in the Jiapigou area. The 2.59–2.53 Ga supracrustal rocks are mainly distributed in the Jiapigou granitoid-greenstone belt (Guo et al., 2015, 2016). The Neoarchean granitoids in the southern Jilin terrane include earlier TTG suite and later potassic granite and quartz diorite. Geochronological evidence indicates that the TTGs mainly formed at 2.6–2.5 Ga, with minor magmatism at 2.78–2.6 Ga (Bao et al., 2022; Wu et al., 2021). The 2.78–2.6 Ga TTG rocks are mostly preserved as relict fragments within the younger 2.6–2.5 Ga rocks in the Baishan and Helong areas (Bao et al., 2022; Liu et al., 2025; Wu et al., 2021). Some researchers suggest that these rocks may represent a nearly east-west trending island arc magmatic belt (Bao et al., 2022). The 2.6–2.5 Ga TTG rocks are the dominant component of the Southern Jilin crystalline basement, widely distributed in the Tonghua, Jingyu, Baishan, Helong, and Jiapigou regions. The genesis of these rocks has been extensively debated, with the prevailing view suggesting that they formed through partial melting of a mafic precursor, which may have included both thickened lower crust (Li et al., 2023; Shan et al., 2019) and subducted slabs (Guo et al., 2017; Shan et al., 2019). Potassic granites were emplaced slightly later than the TTG rocks, around 2.53–2.47 Ga, and are primarily exposed in the Huadian, Jingyu, Tonghua, and Baishanhu regions. These granites display weak deformation to massive structures and intrude both the TTG and supracrustal rocks. They are generally considered products of crustal recycling in a thickened lower crust environment (Guo et al., 2018; Li et al., 2023; Liu et al., 2024). Recently, some studies have identified inherited zircons with ages of 3.5 Ga and 3.2 Ga within the potassic granites from the Baishanhu area. Coupled with Hf isotope data, these findings suggest the presence of an ancient continental nucleus in the Baishanhu region (Liu et al., 2024). During the middle-late Jurassic, the northern margin of the southern Jilin terrane experienced significant ductile deformation related to closure of the Mongol-Okhotsk Ocean (Huang et al., 2022c).

3 Field investigation and petrography

This study focuses on Neoarchean potassic granites within the Baishanhu region, which intrude the early-formed Neoarchean TTG rocks and lack post-crystallization deformation. Field investigations reveal numerous mafic enclaves within the potassic granites (**Fig. 2**) that are up to tens of centimeters in diameter. Contacts between mafic enclaves and host granites show evidence of hybridization. In particular, heterogeneous gradational zones show interdigestion of weakly foliated to unfoliated granite with hybrid rock containing mafic enclaves (**Fig. 2h, i**). These zones host granitoids (granodiorite and quartz diorite) with linear mineral arrangement indicative of magma mixing processes. To decipher the petrogenesis of each lithology and determine the potential role of magma mixing, we collected various samples: (1) potassic granites without mafic enclaves; (2) mafic enclave samples from potassic granite interiors; and (3) granodiorite and quartz diorite from the transitional domains between potassic granites and mafic enclaves.

The potassic granites are predominantly syenogranite and monzogranite. The former contains microcline (45-55%), plagioclase (20-25%), quartz (15-20%), biotite (3-5%), and small amounts of accessory minerals (**Fig. 3a**), whereas the latter contains microcline (35-40%), plagioclase (30-35%), quartz (20-25%), biotite (2-5%), and additional accessory minerals (<5%) (**Fig. 3b**). Microcline and plagioclase in both lithologies exhibit subhedral to anhedral shapes with grain sizes of 1–3 mm. Quartz is predominantly interstitial between feldspars, typically being less than 1 mm in size.

Plagioclase shows partial kaolinization or sericitization (**Fig. 3a, b**).

The mafic enclaves predominantly consist of amphibolite and hornblendite. Amphibolite samples comprise hornblende (40-45%) and plagioclase (50-55%), with minor clinopyroxene, biotite, and quartz (**Fig. 3c, d**). These hornblende and plagioclase grains are subhedral and small (<1 mm), each having undergone a certain degree of chloritization and kaolinization, respectively. In contrast, hornblendite samples are mostly amphibole (85–90%) with minor plagioclase (5–10%). Amphibole in the hornblendite ranges in composition from actinolite to hornblende, and is significantly affected by chloritization (**Fig. 3e**). Additionally, small quantities of biotite, pyroxene, and ilmenite are present in these mafic enclaves.

The hybrid rocks between host potassic granite and mafic enclave are composed mainly of granodiorite and diorite. Specifically, granodiorite samples share mineral assemblages similar to the monzogranites, but have less microcline and more plagioclase and mafic minerals. These granodiorites contain plagioclase (35-40%), quartz (20-25%), hornblende (15-20%), biotite (5-10%), and microcline (5-10%) (**Fig. 3f-j**). In contrast, diorite samples contain more plagioclase and mafic minerals (e.g. biotite and hornblende), but lack microcline and quartz (**Fig. 3k, l**). Notably, small mafic mineral accumulations composed of biotite, hornblende, and clinopyroxene are observed within the granodiorite and diorite samples (**Fig. 3f-l**).

4 Results

4.1 Zircon U-Pb dating and Hf isotopes

In this study, we selected two potassic granite samples (23HX20-11 and 21LJ25-2), three mafic enclave samples (21LJ25-4, 21LJ26-4, and 23HX20-2), and two granodiorite samples (21LJ26-2 and 23HX20-7) for U–Pb dating. Additionally, 73 zircons with concordant ages were selected to analyze for Lu–Hf isotopes. The U–Pb and Lu–Hf isotope dating results are presented in **Table S1 and Table S2**, respectively.

4.1.1 Potassic granites (23HX20-11 and 21LJ25-2)

Zircon grains from Sample 23HX20-11 are 100 to 200 μm in size, and CL images reveal clear core–rim structures. Cores exhibit distinct concentric oscillatory zones, indicating an acidic magmatic origin (**Fig. 4a, b and Fig. S2a**), although rims lack internal structures and are too narrow for analysis. Based on U–Pb dating ages, these zircons can be classified into two groups: (1) 10 zircons yield variable $^{207}Pb/^{206}Pb$ ages (3350–2700 Ma) (**Fig. 4a**), likely inherited from the source rocks or captured during magma ascent; (2) the other 13 zircons yield relatively similar $^{207}Pb/^{206}Pb$ ages of 2524–2450 Ma (**Fig. 4b**), with an upper intercept age and a weighted mean age of 2517 ± 11 Ma (MSWD= 0.37) and 2510 ± 19 Ma (MSWD= 0.08), respectively. The upper intercept age (2517 ± 11 Ma) is accepted as the crystallization age. Thirteen zircons were further analyzed for Lu–Hf isotopes. Among them, 10 zircons with ages *ca.* 2.5 Ga yielded variable $^{176}Hf/^{177}Hf$ ratios (0.280964–0.281298), $^{176}Lu/^{177}Hf$ ratios (0.000516–0.001370), and $\varepsilon_{Hf(t)}$ values (-8.4 to 2.9) (**Table S2 and Fig. 5**). The two-stage Hf model ages (T_{DM}^2) of these *ca.* 2.5 Ga zircons range from 3523 to 2834 Ma (**Table S2**). Additionally, the other three inherited zircons (3.2–3.0 Ga) yield $^{176}Hf/^{177}Hf$ ratios (0.280649–0.280957) and $^{176}Lu/^{177}Hf$ ratios (0.001172–0.003292), with $\varepsilon_{Hf(t)}$

values of -10.3 to 0.6 and ancient T_{DM}^2 ages (3628–3333 Ma).

Zircon grains from Sample 21LJ25-2 are 100–300 μm in size (**Fig. S2b**). Most grains exhibit concentric oscillatory zones and high Th/U ratios (0.31–1.37) (**Fig. 4c**), indicating a magmatic origin. Thirteen zircons from Sample 21LJ25-2 yield $^{207}Pb/^{206}Pb$ ages of 2519–2504 Ma (**Fig. 4c**). They yield an upper-intercept age at 2514 ± 3 Ma (MSWD = 1.01), which aligns with the weighted mean age (2510 ± 5 Ma; MSWD = 0.33). Two older zircons (2742 and 2634 Ma) were likely inherited from their source rocks or captured during magma ascent. The upper intercept age (2514 ± 3 Ma) is accepted as the crystallization age of Sample 21LJ25-2. Eight zircons were further analyzed for their Lu–Hf isotopes. Compared to Sample 23HX20-11, the zircons from Sample 21LJ25-2 exhibit relatively restricted $^{176}Hf/^{177}Hf$ ratios (0.281130–0.281235) and sub-chondrite $\varepsilon_{Hf(t)}$ values (-0.7 to -3.3), with T_{DM}^2 ages of 3049–3210 (**Table S2 and Fig. 5**).

4.1.2 Amphibolites (21LJ25-4, 21LJ26-4, and 23HX20-2)

Zircon grains from the amphibolite samples exhibit broad or banded zoning morphologies (**Fig. 4d-f and and Fig. S2c-e**) and high Th/U ratios (0.19–1.45), they are suggested to be magmatic zircons. Twenty-one zircons from Sample 21LJ25-4 yield $^{207}Pb/^{206}Pb$ ages of 2567–2508 Ma (**Fig. 4d**), with an upper intercept age of 2512 ± 19 Ma. This age represents the crystallization age. Fifteen zircons from Sample 21LJ26-4 were analyzed; they display $^{207}Pb/^{206}Pb$ ages of 2530–2509 Ma (**Fig. 4e**). These analyses yield an upper intercept age of 2514 ± 7 Ma and a weighted mean age of 2514 ± 13 Ma. Similar to the other two amphibolite samples, 17 analyses of zircon from

Sample 23HX20-2 yield $^{207}Pb/^{206}Pb$ ages of 2518–2500 Ma. These zircons have an upper intercept age of 2513 ± 10 Ma and a weighted mean age of 2509 ± 12 Ma (**Fig. 4f**), with the former regarded as the crystallization age of Sample 23HX20-2. In summary, these amphibolite samples and the monzogranite samples have similar crystallization ages of *ca.* 2510 Ma.

Thirty zircon cores from the amphibolite samples (21LJ25-4, 21LJ26-4, and 23HX20-2) were analyzed for their Lu–Hf isotopes. Among them, zircon grains from Sample 21LJ26-4 exhibit restricted ranges in radiogenic Hf isotope compositions, with $^{176}Hf/^{177}Hf$ ratios of 0.281256–0.281422 and $\varepsilon_{Hf(t)}$ values of 2.0 to 4.2 (**Table S2 and Fig. 5**). The $T_{DM}{}^{1}$ ages of these zircons range from 2748 to 2667 Ma. In contrast, zircons from Samples 21LJ25-4 and 23HX20-2 display variable $^{176}Hf/^{177}Hf$ ratios of 0.281138–0.281385) and $\varepsilon_{Hf(t)}$ values of -4.8 to 1.8 (**Table S2 and Fig. 5**).

4.1.3 Granodiorite (21LJ26-2 and 23HX20-7)

Concentric oscillatory zones (**Fig. 4g and Fig. S2f-g**) and high Th/U ratios (0.31–1.07) of zircon grains from 21LJ26-2 indicate a magmatic origin. Fifteen relatively concordant zircons from Sample 21LJ26-2 display $^{207}Pb/^{206}Pb$ ages of 2535–2495 Ma (**Fig. 4g**). They yield a weighted mean age of 2518 ± 6 Ma and an upper intercept age of 2517 ± 10 Ma. In addition, two older zircons have $^{207}Pb/^{206}Pb$ ages of 2655 Ma and 2699 Ma, and so are likely to be inherited or captured. Sample 21LJ26-2 is therefore interpreted to have crystallized at 2518 ± 6 Ma. Eight magmatic zircons show radiogenic Hf isotopes, with restricted $^{176}Hf/^{177}Hf$ ratios (0.281236–0.281340) and $\varepsilon_{Hf(t)}$

values (0.8–3.9) (**Table S2 and Fig. 5**). They yield T_{DM}^1 and T_{DM}^2 ages of 2795–2675 Ma and 2961–2773 Ma, respectively. Another older zircon (2654 Ma) also displays radiogenic Hf isotopes, with a $^{176}Hf/^{177}Hf$ ratio of 0.281313 and an $\varepsilon_{Hf(t)}$ value of 5.3 (**Table S2**).

Seventeen zircons from Sample 23HX20-7 exhibit broad or oscillatory zoning patterns (**Fig. 4h**) and high Th/U ratios (0.19–1.35). These characteristics suggest a magmatic origin for these zircons. They yield $^{207}Pb/^{206}Pb$ ages of 2519–2471 Ma and an upper intercept age of 2513 ± 7 Ma (**Fig. 4h**). The upper-intercept age is approximately consistent with the weighted mean age (2509 ± 11 Ma). Thus, the granodiorite sample 23HX20-7 is interpreted to have formed at 2513 ± 7 Ma. Thirteen zircons were further analyzed for their Hf isotopes. In contrast to Sample 21LJ26-2, most zircons from Sample 23HX20-7 exhibit unradiogenic Hf isotopes, with $^{176}Hf/^{177}Hf$ ratios of 0.281014–0.281259 and variable $\varepsilon_{Hf(t)}$ values of -6.6–1.3 (**Table S2**). Their T_{DM}^2 ages range from 3411 to 2928 Ma.

4.2 Whole-rock geochemistry and Nd isotopes

Detailed results of whole-rock geochemistry and Nd isotopes are presented in **Table S3 and Table S4**, respectively.

4.2.1 Potassic granites (monzogranite and syenogranite)

The potassic granite samples display the following major oxide compositions: high SiO_2 (69.21–72.19 wt. %), Al_2O_3 (13.58–14.50 wt. %), and total alkalis (K_2O+Na_2O) (7.16–8.96 wt. %), but low MgO (0.41–1.56 wt. %), TFe_2O_3 (0.89–2.76 wt. %), and

CaO (1.29–1.82 wt. %). These samples plot within the granite field on the TAS diagram (**Fig. 6a**) and can be classified as peraluminous series with A/CNK values of 1.03–1.08 (**Fig. 6b**). Furthermore, they fall into the category of calc-alkaline granites (**Fig. 6c**). The monzogranite samples exhibit elevated total REE concentrations of 80–198 ppm with positive Eu anomalies (Eu/Eu* = 1.1–2.0). They also possess high $(La/Yb)_N$ ratios (33.0–63.8) and low $(Gd/Yb)_N$ ratios (2.00–4.15). These monzogranites are enriched in light rare earth elements (LREE) and large-ion lithophile elements (LILEs; e.g., Rb, Sr, and Ba), Th, and U, but depleted in heavy rare earth elements (HREE) and high field strength elements (HFSEs; e.g., Nb, Ta, and Ti) (**Fig.7a, b**). Additionally, the monzogranites display high Sr/Y ratios (17.5–87.2), and low Cr (7.45–32.5 ppm), Ni (8.56–29.6 ppm), Co (2.41–8.25 ppm), and V (12.0–39.9 ppm) contents.

4.2.2 Mafic enclaves (amphibolite and hornblendite)

Compared to the coeval monzogranites, the amphibolite samples exhibit lower SiO_2 (48.25–54.46 wt. %) but higher MgO (4.49–12.12 wt. %), TFe_2O_3 (8.97–13.74 wt. %), and CaO (5.48–10.58 wt. %) contents. Their Mg# values range from 48 to 64. The amphibolite samples also show variable TiO_2 (0.55–1.60 wt. %) and Al_2O_3 (8.72–16.11 wt. %). They are compositionally classified as gabbro or gabbroic diorite (**Fig. 6a**) and belong to the calc-alkaline magma series (**Fig. 6d**). Most amphibolite samples exhibit high total REE concentrations (269–384 ppm, except for one analysis of 64 ppm) and slight enrichment in LREE (**Fig. 7c**). These amphibolites exhibit low $(La/Yb)_N$ ratios (3.68–20.0, average of 10.4) and negative Eu anomalies (Eu/Eu* = 0.39–0.96). Notably, the amphibolites display distinct depletion in HREE (e.g., Yb, Lu, Y), HSFE (e.g., Nb, Ta, and Ti), and Sr (**Fig. 7d**). Additionally, they exhibit high concentrations of Cr (151–580 ppm, except for one analysis of 20.5 ppm), Ni (39.9–253 ppm), Co (24.6–50.2 ppm), and V (136–330 ppm). The amphibolite samples share similar Nd isotopic compositions, with initial ^{143}Nd/^{144}Nd ratios ranging from 0.509251 to 0.509523 and variable $\varepsilon_{Nd(t)}$ values (-2.5 to 2.8) (**Table S4**). The Nd T_{DM}^1 and T_{DM}^2 ages span from 3093 to 2786 Ma and 3364 to 2724 Ma, respectively (**Table S4**).

In contrast to amphibolite samples, the hornblendite samples have similar SiO_2 (50.01–50.18 wt. %) and TFe_2O_3 (11.77–12.96 wt. %), but exhibit higher MgO (16.18–16.61 wt. %), CaO (11.07–11.44 wt. %), and Mg# values (71–74), along with lower TiO_2 (0.32–0.43 wt. %) and Al_2O_3 (4.76–4.97 wt. %) contents (**Table S3**). They plot in the gabbro field on a SiO_2 *versus* (K_2O+Na_2O) diagram (**Fig. 6a**) and belong to tholeiite magma series (**Fig. 6d**). Similar to the amphibolites, they display high total REE contents (112–213 ppm), low $(La/Yb)_N$ ratios (7.35–9.31), and negative Eu anomalies (Eu/Eu* = 0.40–0.46). Additionally, the hornblendites show slight enrichment in LREE, Rb, Zr, and Hf, but depletion in Nb, Ta, Ti, Sr, and HREE, (**Fig. 7c, d**). Notably, they have high Cr (1575–1577 ppm), Ni (340–373 ppm), Co (45.5–52.7 ppm), and V (93.9–112 ppm).

4.2.3 Sanukitoids (granodiorite and diorite)

The granodiorite samples exhibit high SiO_2 (65.30–65.99 wt. %), Al_2O_3 (14.47–15.02 wt. %), and total alkaline (Na_2O+K_2O) (6.72–8.08 wt. %), but low TFe_2O_3 (4.33–4.99 wt. %), MgO (1.97–2.02 wt. %), and CaO (2.74–3.38 wt. %) contents (**Table S3**). They have Mg# values between 44 and 47, and plot in the quartz monzonite and granodiorite fields on a SiO_2 *versus* (K_2O+Na_2O) diagram (**Fig. 6a**). They are metaluminous (A/CNK = 0.87–0.95) and belong to the calc-alkaline magma series (**Fig. 6b, c**). In comparison, the diorite sample (23HX20-9) exhibits slightly lower SiO_2 (60.96 wt. %), higher TFe_2O_3 (7.12 wt. %), MgO (2.86 wt. %), and CaO (4.52 wt. %) contents, also aligning with the metaluminous and calc-alkaline series (**Fig. 6b, c**). Both granodiorite and diorite samples share similar trace element characteristics, including high total REE contents (161–436 ppm), Sr (375–432 ppm), and Ba (537–1439 ppm), along with moderate Y (15.3–25.2 ppm) and Yb (1.23–1.97 ppm) contents. They exhibit variable $(La/Yb)_N$ ratios (16.4–71.6) and Sr/Y ratios (16–27), with negative Eu anomalies (Eu/Eu* = 0.59–0.81). Analogous to monzogranite samples, the granodiorite and diorite samples are enriched in LREE and LILE (e.g., Ba and Rb), while showing depletion in HREE and HFSE (e.g. Nb, Ta, and Ti) (**Fig. 7a, b**). Furthermore, these rocks display geochemical features akin to typical sanukitoid rocks and plot within the sanukitoid region on a discrimination diagram (**Fig. 8**).

5 Discussion

5.1 Diverse Late Neoarchean magmatism in the southern Jilin terrane

The southern Jilin terrane witnessed intense magmatic activity during 2.6–2.5 Ga, leading to formation of a highly diverse set of lithologies, including TTG, potassic granite (monzogranite, syenogranite), quartz diorite, mafic dyke, and volcanic rocks (Guo et al., 2018; Li et al., 2023; Shan et al., 2023), which were variably metamorphosed. Similar diverse Neoarchean magmatic suites have been documented in other cratons (e.g. the Dharwar Craton), and are interpreted to result from the partial melting of heterogeneous sources involving enriched mantle and deep crustal components (Dey et al., 2016; Jayananda et al., 2000, 2018, 2020; Moyen et al., 2003). Their formation is typically attributed to the onset of subduction and crustal reworking driven by horizontally dominated plate tectonic processes (Laurent et al., 2014). Within the southern Jilin terrane, Neoarchean magmatism is predominantly represented by transitional TTG, inferred to have formed around 2.55–2.52 Ga (Li et al., 2023). These Neoarchean TTG rocks likely originated from partial melting of thickened mafic lower crust (Li et al., 2023; Wu et al., 2021) or subducted oceanic slabs (Guo et al., 2017; Shan et al., 2022). Evidence of mafic magmatic and volcanic activity is given by metavolcanic rocks (e.g. amphibolite and biotite schist), with minor amphibolite/hornblendite enclaves occurring within the TTG or potassic granites. Notably, the mafic metavolcanic rocks are approximately contemporaneous with the TTGs (Guo et al., 2016). An additional series of 2.52–2.50 Ga potassic granitoids and quartz diorite have been identified in the Jilin terrane. These granitoids formed slightly later than the TTG and metavolcanic rocks and show structural relationships indicating formation related to regional metamorphism. The potassic granitoids and quartz diorite are thus considered to represent intraplate or post-collisional magmatism (Guo et al., 2018). Moreover, recent studies have reported the emplacement of mafic dykes in the southern Jilin terrane, temporally coincident with the intrusion of potassic granitoids (Cheng et al., 2024). Our study further reveals a suite of potassic granitoids (syenogranite and monzogranite), granodiorite, quartz diorite, and mafic enclaves (amphibolite and hornblendite) from the southern Jilin terrane. Several geochronological studies have shown that these igneous rocks crystallized around 2.51 Ga (**Fig. 4**). Together, these lithologies indicate that the Jilin terrane experienced diverse magmatism during NCC cratonization in the late Neoarchean.

5.2 Petrogenesis of potassic granite: partial melting of thickened crust

The use of whole-rock geochemistry to interpret the metamorphic and magmatic evolution of the continental crust requires understanding of the potential for trace element mobility. A brief assessment of this is given in the **Supplementary material** and the following discussion only involves elements considered to have a low mobility.

The geochemical characteristics of the potassic granite samples in this study are consistent with those of typical K-rich biotite granites and two-mica granites, as evidenced by high SiO_2 content, K_2O/Na_2O ratios and A/CNK values (Laurent et al., 2014). These samples display distinctive Sr/Y ratios (17.5-87.2) and $(La/Yb)_N$ ratios (33.0-63.8). Additionally, their low Mg# values and low concentrations of Cr (7.45-32.5 ppm) and Ni (8.56-29.6 ppm) suggest that the magma were originated primarily from crustal sources, with minimal to no contribution from the mantle. Several hypotheses have been proposed regarding the petrogenesis of potassic granite in Archean terranes. One view suggests that these granites formed through the fractional crystallization of TTG magmas (Kleinhanns et al., 2003; Wang et al., 2020); however, other workers argue that they are derived from the partial melting of pre-existing TTG rocks (Laurent et al., 2014; Sun et al., 2020a, 2024; Vijaya Kumar et al., 2011) or partial melting of lower to middle crust with contributions from mantle-derived components (Dey et al., 2016; Jayananda et al., 2000; Joshi et al., 2016). Fractional crystallization typically leads to a positive correlation between melt SiO_2 content and ratios such as Dy/Yb, Sr/Y, and La/Yb, while a negative correlation with HREE and Y (Macpherson et al., 2006). However, this study, as well as previous research on these potassic granites (Li et al., 2023), did not observe such trends. This suggests that fractional crystallization may not be a valid explanation for the formation of potassic granites in this region.

Dey et al. (2016) categorized potassium-rich granitic rocks into two types: Closepet-type granites and K-rich granitoids. Closepet-type granites are interpreted to have formed through partial melting of the lower to middle crust with mantle input. They are characterized by variable SiO_2 content and relatively high concentrations of MgO (2.44–3.22 wt. %), Cr (82–124 ppm), and Ni (25–45 ppm), features typically indicative of mantle-derived contributions. In contrast, K-rich granitoids exhibit higher SiO_2 and lower MgO, Cr, and Ni contents, suggesting an origin dominated by partial melting of crustal materials, with minimal or no mantle involvement.

The potassic granites in this study display distinctly low MgO (0.41–1.56 wt. %), Cr (7.45–32.5 ppm), Ni (8.56–29.6 ppm), and Yb (0.39–0.54 ppm) concentrations. These geochemical characteristics closely resemble those of the K-rich granitoids in the Dharwar Craton, supporting an origin primarily from crustal melting. This interpretation aligns with recent studies (Li et al., 2023; Sun et al., 2024) that attribute the formation of numerous high-K granite in southern Jilin to crustal reworking process. Although mafic magmatic enclaves (MMEs) are observed in some outcrops, indicating localized mafic magma injection into potassic granites, the dominant lithology in this region is syenogranite (Li et al., 2023), which typically lacks MMEs and exhibits massive structures. Petrographic analyses suggest that where MMEs do occur, interaction with the host potassic granite are primarily through mechanical mingling rather than chemical mixing. These limited-scale interactions are insufficient to generate regionally extensive and homogeneous hybridized granite plutons. Moreover, the high Sr/Y and $(La/Yb)_N$ ratios observed in the potassic granite cannot be explained by mixing with the mafic enclaves. The mafic enclaves themselves display lower Sr/Y (0.6–16.5) and $(La/Yb)_N$ (3.68–20) ratios (**Table S3**). If magma mixing were the primary process, the parental magma of the potassic granites would require higher Sr/Y and $(La/Yb)_N$ ratios. Taken together, our findings strongly indicate that late Neoarchean high-K granitic rocks in the southern Jilin terrane formed via crustal melting, with minimal mantle input.

The potassic granite samples have relatively low A/CNK values (1.03~1.08), which are consistent with I-type granite, indicating derivation from a magmatic source rock (**Fig. 6b**). Based on a $3 \times CaO–Al_2O_3/(FeO^T+MgO)–5 \times (K_2O/Na_2O)$ diagram (**Fig. 9a**), the source rocks for these potassic granites, as well as those reported previously, are likely tonalites, with some sedimentary contributions to the melt source. The variability in zircon Hf isotopes further reflects the heterogeneity of the source (**Fig. 5**). Previous studies have shown that HREE, such as Y and Yb, are typically enriched in amphibole and garnet, while Sr and Eu are concentrated in plagioclase. Consequently, the Sr/Y and $(La/Yb)_N$ ratios of igneous rocks are often used as important indicators of the depth of partial melting. High-pressure conditions are favorable for the formation of partial melts with high Sr/Y values (Profeta et al., 2015). The observed enrichment of Sr, depletion of Y and Yb, and positive Eu anomalies of the potassic granites suggest that partial melting occurred under conditions where the residue was rich in garnet but lacked plagioclase (Moyen and Stevens, 2006; Palin et al., 2016), implying pressures exceeding 9–10 kbar, equivalent to 28-30 km depth within the crust. Furthermore, phase equilibrium modelling by Li et al. (2023) supports the presence of a thickened crust in the southern Jilin terrane during the late Neoarchean. Integrating the available evidence, the potassic granites in the southern Jilin terrane are more likely products of partial melting of ancient TTG under a thickened crustal setting.

5.3 Petrogenesis of mafic enclaves: partial melting of lithospheric mantle and subsequent crystallization fractionation

The amphibolite and hornblendite samples both exhibit low SiO_2 and high MgO, TFe_2O_3, Cr, and Ni contents, indicative of a mantle origin. In comparison to the amphibolites, the hornblendites display even higher MgO contents (12.12–16.61 wt. %), similar to those observed in komatiitic basalts. Given that the hornblendites are predominately composed of amphiboles, they likely represent altered Mg-rich cumulate phases. Moreover, both the amphibolite and hornblendite samples exhibit distinct fractional crystallization trends on a La/Sm–La diagram (**Fig. 10a**). The TiO_2, Fe_2O_3, CaO, Ni, and Cr contents in these mafic samples also show good linearity with MgO content (**Fig. 10b–f**), suggesting fractional crystallization involving olivine or pyroxene (Zhang et al., 2012).

To further constrain the fractionation process, we simulated magmatic equilibrium crystallization process using Rhyolite-MELTS (version 1.0.2; Gualda et al., 2012) under various pressures (0.2, 0.6, 1.0, 1.4, 1.8, and 2.2 GPa) using the average content of the amphibolite samples as the primary component. Previous research has shown that most Archean granitoids exhibit magmatic fO_2 values within 1 log unit of the fayalite–magnetite–quartz (FMQ) buffer (with a median FMQ of -0.1 ± 1.1), and Archean mantle-derived magmas may be even more reducing than Archaean granitoids (Ge et al., 2023). Consequently, we selected ΔFMQ as the simulated oxygen fugacity. Our results show that the major oxides (e.g., Al_2O_3, SiO_2, CaO, and TiO_2) in the hornblendites match the evolution trend of 25–45% solid phase fractionation under pressure conditions ranging from 0.6 to 2.2 GPa (**Fig. 11**). High-pressure fractionation (1.4–2.2 GPa) could lead to the crystallization of garnet during the early stages of equilibrium crystallization (**Fig. 12**). However, neither garnet nor garnet pseudomorphs were observed in our samples. Instead, fractionated solid cumulate phases under lower pressures (0.6–1.0 GPa) are primarily composed of clinopyroxene with minor olivine (**Fig. 12**), which is consistent with the mineral assemblage and geochemical features observed here, for example the linear relationship between MgO and Fe_2O_3, CaO, Ni, and Cr. In conclusion, the parental magmas of these mafic enclaves experienced low-pressure fractionation, generating 25–45% clinopyroxene and olivine as cumulus minerals. These accumulated phases subsequently underwent transformation into hornblendites through reaction-replacement processes, consuming clinopyroxene and olivine. This transformation typically occurs during the crystallization of mafic arc magmas and requires that the melts reacting with clinopyroxene are not co-genetic (Smith, 2014). Considering the effects of magma mixing/mingling discussed in Section 5.4, we propose that the interaction between potassic granitic melts and injected mafic magmas disrupted the original magmatic equilibrium. The H_2O released during the progressive crystallization of granitic magma likely facilitated the transformation of cumulate phases into amphibolite.

Previous studies suggest that the ratios of incompatible trace elements (such as Nb/La, La/Yb, Th/Yb, and Nb/Yb) remain relatively stable during magmatic crystallization and fractionation (Hofmann, 1988; Ma et al., 2021; Singer et al., 2007; Zhao et al., 2019). Consequently, even though the mafic samples in our study have undergone significant fractionation, their trace element ratios are still considered useful for constraining their magma sources. The Nb/La *versus* La/Yb diagram indicates a lithospheric mantle origin for all the mafic samples of this study (**Fig. 13a**; Zafar et al., 2020). Furthermore, the Sm/Yb *versus* Sm diagram provides additional insight, illustrating that the primary magmas of these mafic samples likely resulted from partial melting of spinel-garnet lherzolite. The observed depletion of HFSE, such as Nb, Ta, and Ti, coupled with the enrichment of LILE, including Rb, Ba, and K, further suggests an enriched source region. This interpretation aligns with the negative $\varepsilon_{Hf(t)}$ and $\varepsilon_{Nd(t)}$ values in our samples. Lastly, the $(Nb/La)_N$ *versus* $(Hf/Sm)_N$ diagram provides additional evidence that the lithospheric mantle underwent metasomatism primarily by fluid-driven rather than melt-driven processes (**Fig. 13c**; La Flèche et al., 1998).

In summary, the primary magmas of these mafic enclaves were generated from low-degree partial melting of an enriched lithospheric mantle. Subsequently, these primary mafic magmas underwent significant clinopyroxene and olivine fractionation under low-pressure conditions and were later hydrated to form amphibole-rich assemblages.

5.4 Magma mixing origin for sanukitoids

The granodiorite and quartz diorite samples show many characteristics resembling sanukitoids, as illustrated in **Figure 8**. The genesis of sanukitoid is commonly attributed to subduction-related processes (Danyushevsky et al., 2008; Martin et al., 2005; Moyen et al., 2003). Typically, sanukitoids form by the interaction of partial melt derived from a subducted slab with the lithospheric mantle. These rocks typically exhibit relatively low SiO_2 contents (<62 wt.%), moderate K_2O/Na_2O ratios (~0.72), and elevated concentrations of MgO (3.90 ± 1.41 wt.%), Fe_2O_3 (6.75 ± 1.94 wt.%), Ni (54 ppm), and Cr (104 ppm) (Martin et al., 2009). Their Sr and Ba contents consistently exceed 1000 ppm, and they are characterized by high Sr/Y ratios, indicating formation in a high-pressure mantle environment (Moyen, 2011; Moyen and Martin, 2012). However, the studied sanukitoid samples exhibit lower Sr/Y ratios (16–27), indicating melting at relatively low pressures, and thus challenging the likelihood of formation in a subduction zone environment, unless the angle of subduction was extremely low.

Although the geochemical signatures of sanukitoid samples in our study resemble those derived from the partial melting of a metasomatized mantle wedge, several key observations suggest that magma mixing played a dominant role in their formation.

First, the granodiorites and quartz diorites exhibit heterogeneous, gradational contacts with host granites, including complex interdigitation between weakly foliated to unfoliated granitic domains and hybrid rock containing mafic enclaves (**Fig. 2h, i**). Such textural features are characteristic of magma mingling zones (Jayananda et al., 2014). Moreover, these rocks contain abundant oriented mafic microgranular enclaves and basic enclaves (**Fig. 2i**), many of which display chilled margins (**Fig. 2j**), indicating dynamic processes of high-temperature magma injection (Jayananda et al., 2014; Morgavi et al., 2022; Sun et al., 2020b). Further evidence for magma mixing includes disequilibrium textures such as coarse plagioclase grains enclosing microcline cores (**Fig. 3j**), the occurrence of microcline within amphibolite enclaves (**Fig. 3d**), and resorbed surfaces and oscillatory zone in hornblende (**Fig. 3e**). These features strongly support the interpretation that magma mixing was a critical process in the formation of the sanukitoids in this study. Moreover, our geochemical modelling further supports the magma mixing hypothesis (**Figs. 11 and 14**). We used syenogranite sample 23HX20-11 and the average composition of amphibolite samples as proxies for the felsic and mafic endmembers, respectively. The modelling results demonstrate that the major oxides (e.g., SiO_2, MgO, Al_2O_3, CaO, TiO_2, and TFe_2O_3), trace elements (e.g., Ni, V, Co, Sc, Gd, Dy, and Yb), and Sr/Y ratios of the sanukitoids can be accurately reproduced by a mixture of 70–50% syenogranite and 30–50% amphibolite (**Figs. 11 and 14**). The variable zircon $\varepsilon_{Hf(t)}$ values (+3.9 to -6.6) in the sanukitoids provide additional evidence for magma mixing. Furthermore, our modelling suggests that the monzogranite samples were slightly influenced by mixing with a minor proportion

(~10%) of mafic magmas (**Figs. 11 and 14**).

Studies of magma mixing and mingling in the Dharwar Craton have demonstrated a strong correlation between the morphology of mafic enclaves and the crystallization stage of the host magma (Jayananda et al., 2014). This relationship provides valuable insights into similar magmatic processes that occurred in the southern Jilin terrane. When mafic magma intrudes into a low-crystallinity felsic host, the small viscosity contrast facilitates convective mixing, resulting in a homogenized hybrid magma (Barbarin, 2005; Jayananda et al., 2014). However, as the crystallinity of the host magma increases to 30–40%, the growing viscosity difference inhibits mixing and favors mechanical mingling instead. This stage is marked by enclaves with sharp contacts, chilled margins, and compositional gradients. Once the crystallinity exceeds ~70%, the host behaves rheologically as a solid, preventing both mixing and mingling. At this point, mafic magma intrudes primarily through contraction fractures, forming fragmented dikes or dike swarms (Barbarin, 2005; Jayananda et al., 2014). In the southern Jilin terrane, the widespread presence of mafic enclaves and disequilibrium textures in granodiorites and quartz diorites suggests that mingling was the dominant interaction mechanism. The morphological characteristics of the enclaves—ranging from pillowed to angular—and the distribution of contemporaneous mafic dikes indicate that mafic magma was emplaced when the granitic host had reached approximately 30–40% crystallinity. At this stage, the increased viscosity of the partially solidified felsic magma restricted mixing, favoring mechanical mingling and preserving enclave features. Additionally, the presence of multiple generations of Late

Neoarchean mafic dikes in the region (Cheng et al., 2024) points to repeated mafic magma emplacement events, reflecting active crust–mantle interaction likely driven by deep geodynamic processes associated with cratonization.

In conclusion, both petrological and geochemical evidence indicate that the sanukitoids (granodiorite and quartz diorite) of this study are products of magma mingling of coeval mafic and felsic magmas, rather than being directly linked to subduction processes. This finding highlights the complexity of magmatism and emphasizes that diversity in magmatic products does not necessarily correlate with subduction-related arc magmatism (Laurent et al., 2014). Magma mixing and mingling remains a crucial factors in understanding the evolution of magmatic systems within the continental crust (Jayananda et al., 2014).

5.5 Tectonic implications

The geodynamic regimes responsible for the formation and evolution of Archean felsic crust remains a subject of debate. Some scholars argue that modern-style plate tectonics driven by subduction has existed on Earth since at least the Early Archean, but potentially during the Hadean too (Ge et al., 2023; Kusky and Wang, 2022; Sotiriou et al., 2023). By contrast, numerical simulations and comparative planetology has argued that the Archean Earth may have exhibited a collage of lithospheric plates, although they did not show the same degree of horizontal motion as expected from a plate tectonic regime; instead, they were static (or stagnant) and subduction did not operate (Stern et al., 2018). In this latter scenario, where horizontal motion was limited, material and energy exchange between the crust and mantle primarily occurred through vertical processes, such lithospheric dripping or delamination, and crust formation was driven by mantle plume activity (Fischer and Gerya, 2016; Lin and Beakhouse, 2013). Discriminating between these competing scenarios for the Archean Earth requires determining when plate motion and/or subduction began at a global scale. Geological records and geodynamic modeling suggest that the Mesoarchean and Neoarchean were critical periods for global tectonic transitions (Laurent et al., 2014; Liu et al., 2024; Palin et al., 2020; Smart et al., 2016; Tang et al., 2016b). While the timing of initiation of plate tectonics remains debated, extensive rock records from several cratons suggest that subduction was active globally by the Neoarchean, such as the Superior (Lodge, 2016; Polat et al., 2022), Karelian (Heilimo et al., 2010; Kozlov et al., 2021), Dharwar (Kavyanjali et al., 2024; Mohan et al., 2013; Sharma et al., 2019), and Yilgarn (Goscombe et al., 2019; Morris and Kirkland, 2014), indicating a well-established plate tectonic system by this time (Hartnady and Kirkland, 2019; Huang et al., 2022b).

For many years, the NCC was considered an anomaly among ancient cratons due to the scarcity of 2.7 Ga rock records. However, recent studies have reported a 2.7 Ga magmatic belt extending east-west in the northern Liaoning–southern Jilin region (Bao et al., 2022; Liu et al., 2025). Additionally, early Neoarchean metamorphic volcanic rocks related to subduction have been identified in northern Shandong, suggesting a tectonic mechanism driven by asthenosphere upwelling induced by plate subduction (Wang et al., 2024a). Furthermore, substantial evidence for late Neoarchean subduction is preserved across the NCC, including forearc and arc assemblages in the Alxa, Ordos, Fuping, Jianping, eastern Hebei, and Dengfeng regions (Huang et al., 2022a; Ning et al., 2023; Peng et al., 2020; Tang et al., 2016a; Tian et al., 2023; Wang et al., 2024b). Additional indicators include paired metamorphic belts in Dengfeng (Huang et al., 2020), Alpine-style subhorizontal arc-affinity nappe structures (Zhong et al., 2021, 2022), and Neoarchean ophiolitic mélange belt (Ning et al., 2023) and ultrahigh-pressure metamorphic belt (Wu et al., 2022) in eastern Hebei, which further support the presence of horizontal motion and a dominant plate tectonic regime during the late Neoarchean.

Neoarchean metamorphic volcanic rocks in the granite-greenstone belts of Jiapigou and Helong in southern Jilin also exhibit typical arc-related rock assemblages (Guo et al., 2015, 2016). Late Neoarchean potassic granites (e.g., syenogranite and monzogranite) and dioritic rocks (e.g., diorite and quartz diorite) are considered indicators of plate tectonic activity (Guo et al., 2017, 2018; Shan et al., 2019). The mafic enclaves analyzed in this study show geochemical characteristics consistent with arc magmatism, suggesting they originated from partial melting of a lithospheric mantle metasomatized by subduction-related fluids. Oxygen isotopes are a reliable subduction tracer and previous work has indicated an abrupt shift in δ^{18}O values of TTG rocks in the NCC during the late Neoarchean that may be linked to large-scale subduction initiation (Liu et al., 2024). These findings suggest that subduction processes played a significant role in shaping the continental crust of the NCC during the late Neoarchean. Nonetheless, evidence for mantle plume activity, including Neoarchean TTG rocks with mantle-like zircon δ^{18}O values (Wu et al., 2021), counterclockwise P-T-t metamorphic paths (Ge et al., 2003; Liu and Wei, 2020; Wu et al., 2013), presence of widespread dome-and-keel structures within Neoarchean granite-greenstone belts (Zhao et al., 2012), and mafic rocks with ocean island basalt (OIB)-like geochemical signatures (Cheng et al., 2024), suggest that localized mantle plumes may have also contributed to the tectonic evolution of the southern Jilin region.

In summary, our findings suggest that subduction-driven horizontal tectonics (i.e., plate tectonics) was the primary mechanism behind Neoarchean magmatic diversity in the southern Jilin terrane. In particular, processes such as asthenospheric upwelling and lithospheric thinning, triggered by slab breakoff, appear to have played a key role in the final cratonization of the NCC. Slab breakoff facilitated the ascent of asthenospheric mantle material, providing the thermal input needed to partially melt previously metasomatized lithospheric mantle. This process generated significant volumes of mafic magmas, which subsequently underplated the continental crust and resulted in partial melting of preexisting TTG suites, producing potassic magmas (**Fig. 15**). As mafic magmas ascended, they underwent fractional crystallization and eventually mingled/mixed with contemporaneous potassic melts, forming granodiorites and diorites.

Similar Neoarchean magmatic frames have been documented in several other cratons, including the Dharwar, Bundelkhand, Bastar, and Yilgarn cratons (Dey et al., 2016; Dey and Moyen, 2020; Joshi et al., 2016; Rowe et al., 2022). Notably, the Dharwar Craton and the Jilin terrane display similar crustal evolutionary trends, characterized by a progressive transition from sodic TTG suites to transitional TTGs and ultimately to potassic granitoids (Dey et al., 2016). Key rock types—such as sanukitoids, Closepet-type granitoids, and other potassic granitoids—serve as geologic indicators of cratonization in these regions (Dey et al., 2016). In addition, comparable magmatic assemblages have been also identified in the Bundelkhand and Bastar cratons, where they are interpreted to have formed from hybrid sources involving ancient felsic crust and sediment-metasomatized mantle (Dey and Moyen, 2020). This widespread similarity in magmatic and tectonic evolution suggests that late Neoarchean magmatism across these cratons was shaped by common geodynamic processes, possibly related to early supercraton formation. The assembly of late Archean continental crust into supercratons further supports this interpretation (Bleeker, 2003). Three major Neoarchean supercratons have been proposed based on amalgamation and breakup histories: Superia (the Superior, Hearne, and Kola/Karelia cratons), Vaalbara (Kaapvaal and Pilbara cratons), and Sclavia (the Slave, Yilgarn, Zimbabwe, Dharwar, and São Francisco cratons) (Bleeker, 2003). Recent studies suggested that the NCC may also have been part of the Sclavia supercraton, based on evidence such as similar early tectono-thermal histories, ca. 2.7 Ga basaltic volcanism, and synchronous cratonization events (Liu et al., 2025). This hypothesis strengthens the view that magmatic records from the NCC and cratons like Dharwar, Bundelkhand, and Bastar reflect coordinated tectonic processes during late Neoarchean crustal evolution. Collectively, these cratons preserve evidence of microcontinental amalgamation, slab breakoff, and mantle upwelling within a subduction-dominated geodynamic setting (Dey and Moyen, 2020; Jayananda et al., 2020; Joshi et al., 2016). We therefore conclude that large-scale

Neoarchean magmatism was intrinsically linked to the assembly of microcontinental blocks within the Sclavia supercraton. Subduction-accretionary orogenic systems likely played a fundamental role in shaping crustal architecture and driving the eventual stabilization of these cratons.

6. Conclusions

We present the results of detailed petrology, zircon U–Pb geochronology and Hf isotope analyses, whole-rock geochemistry and Nd isotope compositions, and fractionation-mixing modelling, which shed light on the petrogenesis and tectonic environment of the late Neoarchean granitoids and their mafic enclaves from the southern Jilin terrane. The following key conclusions emerge.

(1) Zircon U–Pb dating results reveal that potassic granites, granodiorite, quartz diorite, and their mafic enclaves in the study region share a common crystallization age of approximately 2510 Ma.

(2) The potassic granites resulting from the partial melting of thickened continental crust with minor mantle-derived input, whereas mafic enclaves (amphibolites) originated from partial melting of an enriched lithospheric mantle. Subsequent 25–45% pyroxene-dominated fractional crystallization led to the formation of hornblenditic enclaves. The granodiorite and quartz diorite display sanukitoid affinities, and likely formed through mingling of 70–50% syenogranite and 30–50% amphibolite. These findings contribute to understanding the complex magmatic evolution of the continental crust during the late Neoarchean.

(3) During the late Neoarchean, the southern Jilin terrane was influenced by a

geodynamic regime characterized by microblock amalgamation during subduction-accretion processes. This resulted in a diverse range of magmatic processes, including partial melting, magma mixing, and fractional crystallization.

Acknowledgement

We thank Chief Editor Dicheng Zhua, Prof. Guozheng Sun, and Prof. M. Jayananda for their constructive feedback and insightful suggestions. We are grateful for the assistance from Yachao Dong, Zhongshui Li, and Hongchao Yu during the field investigation. This work is funded by National Natural Science Foundation of China [Grant No. 42172212, 42025204, U2244211, and 42272224].

Appendix A. Descriptions of analytical methods

A.1. LA-ICP-MS zircon U-Pb dating

At Nanjing Hongchuang Geological Exploration Technology Service Co., Ltd., Nanjing, China, we conducted zircon grain separation, target preparation, and cathodoluminescence (CL) imaging. Zircon U–Pb dating was performed using laser-ablation–inductively coupled plasma-mass spectrometry (LA–ICP–MS) at the Key Laboratory of Mineral Resources Evaluation in Northeast Asia, Ministry of Natural Resources, Jilin University, China. Our detailed procedures closely followed those outlined by Lian et al. (2023). For external calibration and quality control, we employed the zircon standards 91500 and Plešovice. The measured zircon standard 91500 yielded a weighted mean ^{206}Pb/^{238}U age of 1061.4 ± 2.6 Ma, consistent with its recommended age of 1062.4 ± 0.4 Ma (Wiedenbeck et al., 1995). Similarly, Plešovice yielded a weighted mean $^{206}Pb/^{238}U$ age of 339.5 ± 1.2 Ma, in agreement with the recommended age of 337.13 ± 0.37 Ma (Sláma et al., 2008). Concordia age diagrams were constructed using Isoplot 4.15 (Ludwig, 2012).

A.2. Zircon Hf isotopic analysis

Based on zircon CL images and the results from zircon U–Pb dating, we selected representative zircons exhibiting high concordance for *in-situ* Lu–Hf isotope analysis. The analysis was conducted at Wuhan Sample Solution Analytical Technology Co., Ltd, Wuhan, China, utilizing a Neptune Plus MC–ICP–MS in conjunction with a Geolas HD excimer ArF laser ablation system. Operating conditions for both the laser ablation system and the MC-ICP-MS instrument, as well as the analytical methodology, closely followed the description by Hu et al. (2012). Plešovice served as an external standard for calibration, optimizing the analysis and test results. Meanwhile, 91500 and GJ-1 functioned as secondary standards to monitor data quality corrections. External precision (2SD) achieved for Plešovice, 91500, and GJ-1 was better than 0.000020, consistently falling within the recommend error range (Zhang et al., 2020). For calculating $\varepsilon_{Hf(t)}$ values, we employed the ^{176}Lu decay constant ($\lambda^{176}Lu$) of 1.865×10^{-11} (Scherer et al., 2001), and chondrite parameters: $^{176}Hf/^{177}Hf = 0.282772$ and $^{176}Lu/^{177}Hf = 0.0332$ (Blichert-Toft and Albarède, 1997). Furthermore, zircon Hf two-stage depleted mantle model ages (T_{DM}^{2}) were calculated using present depleted mantle ratios of $^{176}Hf/^{177}Hf = 0.283251$ and $^{176}Lu/^{177}Hf = 0.0384$ (Griffin et al., 2002), with an assigned $^{176}Lu/^{177}Hf$ value of 0.015.

A.3. Major and trace elements, Nd isotopic analysis

Major and trace element analyses were conducted at Wuhan Sample Solution Analytical Technology Co., Ltd., Wuhan, China. Major elements were analyzed using a Zsx Primus II wavelength-dispersive X-ray fluorescence spectrometer (XRF). Standard curves were derived from national standard materials GBW07103, GBW07105, GBW07111, and GBW071112. The relative standard deviation (RSD) remained below 2%. For trace element analysis, we employed an Agilent 7700e ICP-MS instrument. Quality control was ensured by using standard materials such as GSR-3, RGM-2, BHVO-2, and JA-2, with analysis results consistent with reference values.

The Nd isotopes were analyzed using a Neptune Plus MC–ICP–MS at Nanjing Hongchuang Exploration Technology Service Co., Ltd, China. Operating conditions and analytical procedures followed those described by Li et al. (2023). Data deviations were monitored using the standard material BCR-2. For subsequent Nd isotopic calculation, we adopted the following parameters: the present ^{147}Sm/^{144}Nd and ^{143}Nd/^{144}Nd ratios for chondrite are 0.1967 and 0.512638 (Wasserburg et al., 1981), and 0.2136 and 0.513151 for the depleted mantle (Liew and Hofmann, 1988), respectively. The ^{147}Sm/^{144}Nd ratio for the crust is 0.118 (Jahn and Condie, 1995). The decay constant for Sm is $\lambda^{147}{}_{\mathrm{Sm}} = 6.54 \times 10^{-12}\mathrm{a}^{-1}$ (Lugmair and Marti, 1978).

References:

Bao, H., Liu, S.W., Wan, Y.S., Wang, M.J., Sun, G.Z., Gao, L., Wang, W., Guo, R.R., Fu, J.H., 2022. Neoarchean granitoids and tectonic regime of lateral growth in northeastern North China Craton. Gondwana Research 107, 176-200.

Barbarin, B., 2005. Mafic magmatic enclaves and mafic rocks associated with some granitoids of the central Sierra Nevada batholith, California: nature, origin, and relations with the hosts. Lithos 80, 155-177.

Bleeker, W., 2003. The late Archean record: a puzzle in ca. 35 pieces. Lithos 71, 99-134.

Blichert-Toft, J., Albarède, F., 1997. The Lu-Hf isotope geochemistry of chondrites and the evolution of the mantle-crust system. Earth and Planetary Science Letters 148, 243-258.

Cawood, P.A., Chowdhury, P., Mulder, J.A., Hawkesworth, C.J., Capitanio, F.A., Gunawardana, P.M., Nebel, O., 2022. Secular Evolution of Continents and the Earth System. Reviews of Geophysics 60, e2022RG000789.

Cheng, C., Zhang, J., Liu, J., Liu, Z., Li, Z., Yu, H., Zhao, C., Zhang, H., Dong, Y., 2024. Distinct mafic magmatism of the northeastern Longgang Block: Evidence for coexisting mantle plume and subduction during the Neoarchean North China Craton. Geosystems and Geoenvironment 3, 100286.

Danyushevsky, L.V., Falloon, T.J., Crawford, A.J., Tetroeva, S.A., Leslie, R.L., Verbeeten, A., 2008. High-Mg adakites from Kadavu Island Group, Fiji, southwest Pacific: Evidence for the mantle origin of adakite parental melts. Geology 36, 499-502.

Dey, S., Halla, J., Kurhila, M., Nandy, J., Heilimo, E., Pal, S., 2016. Geochronology of Neoarchaean granitoids of the NW eastern Dharwar craton: implications for crust formation. Geological Society, London, Special Publications 449, 89-121.

Dey, S., Moyen, J.-F., 2020. Archean granitoids of India: windows into early Earth tectonics – an introduction. Geological Society, London, Special Publications 489, 1-13.

Fischer, R., Gerya, T., 2016. Early Earth plume-lid tectonics: A high-resolution 3D numerical modelling approach. Journal of Geodynamics 100, 198-214.

Ge, R.F., Wilde, S.A., Zhu, W.B., Wang, X.L., 2023. Earth's early continental crust formed from wet and oxidizing arc magmas. Nature 623, 334-339.

Ge, W.C., Zhao, G.C., Sun, D.Y., Wu, F.Y., Lin, Q., 2003. Metamorphic P-T Path of the Southern Jilin Complex: Implications for Tectonic Evolution of the Eastern Block of the North China Craton. International Geology Review 45, 1029-1043.

Goscombe, B., Foster, D.A., Blewett, R., Czarnota, K., Wade, B., Groenewald, B., Gray, D., 2019. Neoarchaean metamorphic evolution of the Yilgarn Craton: A record of subduction, accretion, extension and lithospheric delamination. Precambrian Research 335, 105441.

Griffin, W.L., Wang, X., Jackson, S.E., Pearson, N.J., O'Reilly, S.Y., Xu, X.S., Zhou, X.M., 2002. Zircon chemistry and magma mixing, SE China: In-situ analysis of Hf isotopes, Tonglu and Pingtan igneous complexes. Lithos 61, 237-269.

Gualda, G.A.R., Ghiorso, M.S., Lemons, R.V., Carley, T.L., 2012. Rhyolite-MELTS: a Modified Calibration of MELTS Optimized for Silica-rich, Fluid-bearing Magmatic Systems. Journal of Petrology 53, 875-890.

Guo, B.R., Liu, S.W., Chen, X., Wang, W., Guo, R.R., Yan, M., 2018. K-rich granitoid magmatism at the Archean–Proterozoic transition in southern Jilin: Insights into the Neoarchean crustal evolution of the northeastern part of the North China Craton. Gondwana Research 58, 87-104.

Guo, B.R., Liu, S.W., Santosh, M., Wang, W., 2017. Neoarchean arc magmatism and crustal growth in the north-eastern North China Craton: Evidence from granitoid gneisses in the Southern Jilin Province. Precambrian Research 303, 30-53.

Guo, B.R., Liu, S.W., Zhang, J., Wang, W., Fu, J.H., Wang, M.J., 2016. Neoarchean Andean-type active continental margin in the northeastern North China Craton: Geochemical and geochronological evidence from metavolcanic rocks in the Jiapigou granite-greenstone belt, Southern Jilin Province. Precambrian Research 285, 147-169.

Guo, B.R., Liu, S.W., Zhang, J., Yan, M., 2015. Zircon U–Pb–Hf isotope systematics and geochemistry of Helong granite-greenstone belt in Southern Jilin Province, China: Implications for Neoarchean crustal evolution of the northeastern margin of North China Craton. Precambrian Research 271, 254-277.

Hartnady, M.I., Kirkland, C.L., 2019. A gradual transition to plate tectonics on Earth between 3.2 to 2.7 billion years ago. Terra Nova 31, 129-134.

Heilimo, E., Halla, J., Hölttä, P., 2010. Discrimination and origin of the sanukitoid series: Geochemical constraints from the Neoarchean western Karelian Province (Finland). Lithos 115, 27-39.

Hofmann, A.W., 1988. Chemical differentiation of the Earth: the relationship between mantle, continental crust, and oceanic crust. Earth and Planetary Science Letters 90, 297-314.

Hu, Z.C., Liu, Y.S., Gao, S., Liu, W.G., Zhang, W., Tong, X.R., Lin, L., Zong, K.Q., Li, M., Chen, H.H., 2012. Improved in situ Hf isotope ratio analysis of zircon using newly designed X skimmer cone and jet sample cone in combination with the addition of nitrogen by laser ablation multiple collector ICP-MS. Journal of Analytical Atomic Spectrometry 27, 1391-1399.

Huang, B., Johnson, T.E., Wilde, S.A., Polat, A., Fu, D., Kusky, T., 2022a. Coexisting divergent and convergent plate boundary assemblages indicate plate tectonics in the Neoarchean. Nature Communications 13, 6450.

Huang, B., Kusky, T.M., Johnson, T.E., Wilde, S.A., Wang, L., Polat, A., Fu, D., 2020. Paired metamorphism in the Neoarchean: A record of accretionary-to-collisional orogenesis in the North China Craton. Earth and Planetary Science Letters 543, 116355.

Huang, G., Mitchell, R.N., Palin, R.M., Spencer, C.J., Guo, J., 2022b. Barium content of Archaean continental crust reveals the onset of subduction was not global. Nature Communications 13, 6553.

Huang, S.Q., Dong, S.W., Zhang, F.C., Zhang, Y.Q., Shi, W., Müller, W.E.G., 2022c. Timing of the Kaiyuan-Jiapigou shear zone in the northern margin of the North China Craton: Implications for closure of the Mongol-Okhotsk Ocean. Tectonophysics 844, 229626.

Irvine, T.N., Baragar, W.R.A., 1971. A Guide to the Chemical Classification of the Common Volcanic Rocks. Canadian Journal of Earth Sciences 8, 523-548.

Jahn, B.-M., Condie, K.C., 1995. Evolution of the Kaapvaal Craton as viewed from geochemical and Sm-Nd isotopic analyses of intracratonic pelites. Geochimica et Cosmochimica Acta 59, 2239-2258.

Jayananda, M., Aadhiseshan, K.R., Kusiak, M.A., Wilde, S.A., Sekhamo, K.-u., Guitreau, M., Santosh, M., Gireesh, R.V., 2020. Multi-stage crustal growth and Neoarchean geodynamics in the Eastern Dharwar Craton, southern India. Gondwana Research 78, 228-260.

Jayananda, M., Gireesh, R.V., Sekhamo, K.-U., Miyazaki, T., 2014. Coeval Felsic and Mafic Magmas in Neoarchean Calc-alkaline Magmatic Arcs, Dharwar Craton, Southern India: Field and Petrographic Evidence from Mafic to Hybrid Magmatic Enclaves and Synplutonic Mafic Dykes. Journal of the Geological Society of India 84, 5-28.

Jayananda, M., Moyen, J.F., Martin, H., Peucat, J.J., Auvray, B., Mahabaleswar, B., 2000. Late

Archaean (2550–2520 Ma) juvenile magmatism in the Eastern Dharwar craton, southern India: constraints from geochronology, Nd–Sr isotopes and whole rock geochemistry. Precambrian Research 99, 225-254.

Jayananda, M., Santosh, M., Aadhiseshan, K.R., 2018. Formation of Archean (3600–2500 Ma) continental crust in the Dharwar Craton, southern India. Earth-Science Reviews 181, 12-42.

Joshi, K.B., Bhattacharjee, J., Rai, G., Halla, J., Ahmad, T., Kurhila, M., Heilimo, E., Choudhary, A.K., 2016. The diversification of granitoids and plate tectonic implications at the Archaean–Proterozoic boundary in the Bundelkhand Craton, Central India, Crust–Mantle Interactions and Granitoid Diversification: Insights from Archaean Cratons. The Geological Society London, p. 0.

Kamei, A., Owada, M., Nagao, T., Shiraki, K., 2004. High-Mg diorites derived from sanukitic HMA magmas, Kyushu Island, southwest Japan arc: evidence from clinopyroxene and whole rock compositions. Lithos 75, 359-371.

Kavyanjali, K.V., Anilkumar, Y., Santosh, M., Yang, C.-X., Anoop, K.S., Mathew, A., Kwon, S., 2024. A layered gabbro-anorthosite suite from Attappadi: Chemical and isotopic signature of Neoarchean subduction tectonics in the Southern Granulite Terrane, India. Lithos 472-473, 107548.

Kleinhanns, I.C., Kramers, J.D., Kamber, B.S., 2003. Importance of water for Archaean granitoid petrology: a comparative study of TTG and potassic granitoids from Barberton Mountain Land, South Africa. Contributions to Mineralogy and Petrology 145, 377-389.

Kozlov, N.E., Martynov, E.V., Sorokhtin, N.O., 2021. Lapland Granulite Belt–Neoarchean subduction zone in the North-Eastern Baltic shield. Applied Earth Science 130, 241-252.

Kusky, T., Wang, L., 2022. Growth of continental crust in intra-oceanic and continental-margin arc systems: Analogs for Archean systems. Science China Earth Sciences 65, 1615-1645.

Kusky, T.M., Polat, A., Windley, B.F., Burke, K.C., Dewey, J.F., Kidd, W.S.F., Maruyama, S., Wang, J.P., Deng, H., Wang, Z.S., Wang, C., Fu, D., Li, X.W., Peng, H.T., 2016. Insights into the tectonic evolution of the North China Craton through comparative tectonic analysis: A record of outward growth of Precambrian continents. Earth-Science Reviews 162, 387-432.

La Flèche, M.R., Camiré, G., Jenner, G.A., 1998. Geochemistry of post-Acadian, Carboniferous continental intraplate basalts from the Maritimes Basin, Magdalen Islands, Québec, Canada. Chemical Geology 148, 115-136.

Laurent, O., Martin, H., Moyen, J.F., Doucelance, R., 2014. The diversity and evolution of late-Archean granitoids: Evidence for the onset of “modern-style” plate tectonics between 3.0 and 2.5Ga. Lithos 205, 208-235.

Li, J., Shen, B., Li, S., Mao, D., 1998. Geological feature and evolution of the early Precambrian continental crust in northern Liaoning Province and southern Jilin Province. Regional Geology of China 17, 30-38.

Li, J., Shen, B., Li, S., Mao, D., Luo, H., Jin, W., 1996. Geology and geochemistry of Archean granite-greenstone belts in northern Liaoning Province and southern Jilin Province. Geochimica 25, 458-467.

Li, Z.S., Shan, X.L., Liu, J., Zhang, J., Liu, Z.H., Cheng, C.Q., Wang, Z.G., Zhao, C., Yu, H.C., 2023. Late Neoarchean TTG and monzogranite in the northeastern North China Craton: Implications for partial melting of a thickened lower crust. Gondwana Research 115, 201-223.

Lian, G.H., Xu, Z.Y., Liu, Z.H., Liu, J., Li, P.C., Gong, Y.D., Li, S.Q., 2023. Neoarchean to Paleoproterozoic tectonic evolution of the Khondalite Belt in the North China Craton: Constraints from ca. 2.5 Ga and ca. 2.1 Ga charnockites in Zhuozi. Precambrian Research 396, 107167.

Liew, T.C., Hofmann, A.W., 1988. Precambrian crustal components, plutonic associations, plate environment of the Hercynian Fold Belt of central Europe: Indications from a Nd and Sr isotopic study. Contributions to Mineralogy and Petrology 98, 129-138.

Lin, S., Beakhouse, G.P., 2013. Synchronous vertical and horizontal tectonism at late stages of Archean cratonization and genesis of Hemlo gold deposit, Superior craton, Ontario, Canada. Geology 41, 359-362.

Liu, J., Palin, R.M., Mitchell, R.N., Liu, Z., Zhang, J., Li, Z., Cheng, C., Zhang, H., 2024. Archaean multi-stage magmatic underplating drove formation of continental nuclei in the North China Craton. Nature Communications 15, 6231.

Liu, J., Zhang, H., Palin, R.M., Liu, Z., Zhang, J., Cheng, C., Liu, X., Zhao, C., 2025. Early Neoarchean geodynamic regime in the North China Craton: Constraints from 2.7 Ga granitoids in the southern Jilin terrane. Geological Society of America Bulletin 137, 911-931.

Liu, T., Wei, C., 2020. Metamorphic P–T paths and Zircon U–Pb ages of Archean ultra-high temperature paragneisses from the Qian’an gneiss dome, East Hebei terrane, North China Craton. Journal of Metamorphic Geology 38, 329-356.

Lodge, R.W.D., 2016. Petrogenesis of intermediate volcanic assemblages from the Shebandowan greenstone belt, Superior Province: Evidence for subduction during the Neoarchean. Precambrian Research 272, 150-167.

Ludwig, K.R., 2012. User's manual for Isoplot 3.75: A geochronological toolkit for Microsoft Excel. Berkeley Geochronology Center Special Publication 5, 75.

Lugmair, G.W., Marti, K., 1978. Lunar initial 143Nd/144Nd: Differential evolution of the lunar crust and mantle. Earth and Planetary Science Letters 39, 349-357.

Ma, L.T., Dai, L.Q., Zheng, Y.F., Zhao, Z.F., Fang, W., Zhao, K., Xiao, Y.L., Tong, F.T., 2021. Geochemical distinction between altered oceanic basalt-and seafloor sediment-derived fluids in the mantle Source of mafic igneous rocks in Southwestern Tianshan, Western China. Journal of Petrology 62, egab014.

Macpherson, C.G., Dreher, S.T., Thirlwall, M.F., 2006. Adakites without slab melting: High pressure differentiation of island arc magma, Mindanao, the Philippines. Earth and Planetary Science Letters 243, 581-593.

Maniar, P.D., Piccoli, P.M., 1989. Tectonic discrimination of granitoids. Geological society of America bulletin 101, 635-643.

Martin, H., Moyen, J.-F., Rapp, R., 2009. The sanukitoid series: magmatism at the Archaean–Proterozoic transition. Earth and Environmental Science Transactions of the Royal Society of Edinburgh 100, 15-33.

Martin, H., Smithies, R.H., Rapp, R., Moyen, J.F., Champion, D., 2005. An overview of adakite, tonalite–trondhjemite–granodiorite (TTG), and sanukitoid: relationships and some implications for crustal evolution. Lithos 79, 1-24.

Middlemost, E.A., 1994. Naming materials in the magma/igneous rock system. Earth-science reviews 37, 215-224.

Mohan, M.R., Piercey, S.J., Kamber, B.S., Sarma, D.S., 2013. Subduction related tectonic evolution of the Neoarchean eastern Dharwar Craton, southern India: New geochemical and isotopic constraints. Precambrian Research 227, 204-226.

Morgavi, D., Laumonier, M., Petrelli, M., Dingwell, D.B., 2022. Decrypting Magma Mixing in Igneous Systems. Reviews in Mineralogy and Geochemistry 87, 607-638.

Morris, P.A., Kirkland, C.L., 2014. Melting of a subduction-modified mantle source: A case study from the Archean Marda Volcanic Complex, central Yilgarn Craton, Western Australia. Lithos 190-191, 403-419.

Moyen, J.-F., 2011. The composite Archaean grey gneisses: Petrological significance, and evidence for a non-unique tectonic setting for Archaean crustal growth. Lithos 123, 21-36.

Moyen, J.-F., 2019. Archean granitoids: classification, petrology, geochemistry and origin. Geological Society, London, Special Publications 489, 15-49.

Moyen, J.-F., Martin, H., 2012. Forty years of TTG research. Lithos 148, 312-336.

Moyen, J., Stevens, G., 2006. Experimental constraints on TTG petrogenesis: implications for Archean geodynamics. Geophysical Monograph-American Geophysical Union 164, 149.

Moyen, J.F., Martin, H., Jayananda, M., Auvray, B., 2003. Late Archaean granites: a typology based on the Dharwar Craton (India). Precambrian Research 127, 103-123.

Nebel, O., Capitanio, F.A., Moyen, J.F., Weinberg, R.F., Clos, F., Nebel-Jacobsen, Y.J., Cawood, P.A., 2018. When crust comes of age: on the chemical evolution of Archaean, felsic continental crust by crustal drip tectonics. Philosophical Transactions of the Royal Society A: Mathematical, Physical and Engineering Sciences 376, 20180103.

Ning, W., Kusky, T., Wang, L., Wang, J., Deng, H., Huang, B., Meng, J., Wang, R., Hu, D., Peng, Y., Chen, Z., Zhang, W., 2023. Neoarchean SSZ and MOR ultra-/high-pressure ophiolitic mélanges of the Eastern Hebei Complex, North China Craton: Dynamics of an Archean paleo-subduction zone. Earth-Science Reviews 240, 104403.

Palin, R.M., Santosh, M., Cao, W., Li, S.-S., Hernández-Uribe, D., Parsons, A., 2020. Secular change and the onset of plate tectonics on Earth. Earth-Science Reviews 207, 103172.

Palin, R.M., White, R.W., Green, E.C.R., 2016. Partial melting of metabasic rocks and the generation of tonalitic–trondhjemitic–granodioritic (TTG) crust in the Archaean: Constraints from phase equilibrium modelling. Precambrian Research 287, 73-90.

Peng, H., Kusky, T., Deng, H., Wang, L., Wang, J., Huang, Y., Huang, B., Ning, W., 2020. Identification of the Neoarchean Jianping pyroxenite-mélange in the Central Orogenic Belt, North China Craton: A fore-arc accretional assemblage. Precambrian Research 336, 105495.

Polat, A., Frei, R., Deng, H., Yang, X.-M., Sotiriou, P., 2022. Anatomy of a Neoarchean continental arc-backarc system in the Cross Lake-Pipestone Lake region, northwestern Superior Province, Canada. Precambrian Research 370, 106556.

Profeta, L., Ducea, M.N., Chapman, J.B., Paterson, S.R., Gonzales, S.M.H., Kirsch, M., Petrescu, L., DeCelles, P.G., 2015. Quantifying crustal thickness over time in magmatic arcs. Scientific Reports 5, 17786.

Rickwood, P.C., 1989. Boundary lines within petrologic diagrams which use oxides of major and minor elements. Lithos 22, 247-263.

Rowe, M.L., Kemp, A.I.S., Wingate, M.T.D., Petersson, A., Whitehouse, M.J., van der Riet, C., 2022. Cratonisation of Archaean continental crust: Insights from U–Pb zircon geochronology and geochemistry of granitic rocks in the Narryer Terrane, northwest Yilgarn Craton. Precambrian Research 372.

Scherer, E., Münker, C., Mezger, K., 2001. Calibration of the Lutetium-Hafnium Clock. Science 293, 683-687.

Shan, H., Zhai, M., Lu, X., Chai, D., 2023. Reconstructing the evolution of an ancient continental arc: Implications from the temporally-spatially related shoshonitic to calc-alkaline intrusive magmatism in the North China Craton. Lithos 454-455, 107246.

Shan, H.X., Zhai, M.G., Dey, S., Lu, X.P., 2019. Geochronological and geochemical studies on the granitoid gneisses in the northeastern North China Craton: Insights into the late Neoarchean magmatism and crustal evolution. Precambrian Research 320, 371-390.

Shan, H.X., Zhai, M.G., Lu, X.P., 2022. Petrogenesis delineation of the felsic intrusive rocks in the eastern North China Craton: Implications for crustal evolution and geodynamic regimes. Lithos 422-423, 106728.

Sharma, A., Giri, R.K., Rao, N.C., Rahaman, W., Pandit, D., Sahoo, S., 2019. Arc-related pyroxenites derived from a long-lived Neoarchean subduction system at the southwestern margin of the Cuddapah Basin: geodynamic implications for the evolution of the Eastern Dharwar Craton, southern India. The Journal of Geology 127, 567-591.

Shen, B., Luo, H., Han, G., Dai, X., Jin, W., Hu, X., Li, S., Bi, S., 1994. Archean geology and metallization in Northern Liaoning province and Southern Jilin Province. Geol. Publ. House, Beijing, 1-255.

Singer, B.S., Jicha, B.R., Leeman, W.P., Rogers, N.W., Thirlwall, M.F., Ryan, J., Nicolaysen, K.E., 2007. Along-strike trace element and isotopic variation in Aleutian Island arc basalt: Subduction melts sediments and dehydrates serpentine. Journal of Geophysical Research: Solid Earth 112.

Sláma, J., Košler, J., Condon, D.J., Crowley, J.L., Gerdes, A., Hanchar, J.M., Horstwood, M.S.A., Morris, G.A., Nasdala, L., Norberg, N., Schaltegger, U., Schoene, B., Tubrett, M.N., Whitehouse, M.J., 2008. Plešovice zircon — A new natural reference material for U–Pb and Hf isotopic microanalysis. Chemical Geology 249, 1-35.

Smart, K.A., Tappe, S., Stern, R.A., Webb, S.J., Ashwal, L.D., 2016. Early Archaean tectonics and mantle redox recorded in Witwatersrand diamonds. Nature Geoscience 9, 255-259.

Smith, D.J., 2014. Clinopyroxene precursors to amphibole sponge in arc crust. Nature Communications 5, 4329.

Sotiriou, P., Polat, A., Windley, B., Kusky, T., 2023. Temporal variations in the incompatible trace element systematics of Archean TTGs: Implications for crustal growth and tectonic processes in the early Earth. Earth-Science Reviews 236, 104274.

Stern, R.J., Gerya, T., Tackley, P.J., 2018. Stagnant lid tectonics: Perspectives from silicate planets, dwarf planets, large moons, and large asteroids. Geoscience Frontiers 9, 103-119.

Sun, G., Liu, S., Gao, L., Hu, Y., Guo, R., 2020a. Origin of late Neoarchean granitoid diversity in the Western Shandong province, North China Craton. Precambrian Research 339, 105620.

Sun, G., Liu, S., Li, S., Bao, H., Wang, W., Guo, R., Fu, J., Gao, L., Hu, Y., Wang, X., Yu, S., Dai, L., 2024. Neoarchean granitoid magmatism and geodynamic process in the northeastern North China craton. GSA Bulletin 136, 5091-5108.

Sun, G., Liu, S., Li, S., Kusky, T.M., Hu, F., Bao, H., Gao, L., Hu, Y., Yu, S., Dai, L., Wang, L., Wang, X., 2025. Neoarchean orogenic belt evolution in the northeast North China Craton: Implications for the reconstruction of early Earth's microplates. Precambrian Research 417, 107659.

Sun, S.-S., McDonough, W.F., 1989. Chemical and isotopic systematics of oceanic basalts: implications for mantle composition and processes. Geological Society, London, Special Publications 42, 313-345.

Sun, S.J., Zhang, R.Q., Cong, Y.N., Zhang, L.P., Sun, W.D., Li, C.Y., Ding, X., 2020b. Analogous diagenetic conditions of dark enclave and its host granite derived by magma mixing: Evidence for a post-mixing magmatic process. Lithos 356-357, 105373.

Tang, L., Santosh, M., Tsunogae, T., Teng, X.-M., 2016a. Late Neoarchean arc magmatism and crustal growth associated with microblock amalgamation in the North China Craton: Evidence from the Fuping Complex. Lithos 248-251, 324-338.

Tang, M., Chen, K., Rudnick, R.L., 2016b. Archean upper crust transition from mafic to felsic marks the onset of plate tectonics. Science 351, 372-375.

Tian, G., Yang, M., Song, L., Jia, H., Liu, H., Zhang, S., Zhang, W., Xing, Z., Chen, J., Bai, D., Li, J., 2023. Late Neoarchean plate subduction in Western North China Craton: Evidence from ca. 2.51 Ga to 2.46 Ga basement rocks in Northern Ordos Basin. Precambrian Research 387, 106979.

Vijaya Kumar, K., Ernst, W.G., Leelanandam, C., Wooden, J.L., Grove, M.J., 2011. Origin of ~2.5 Ga potassic granite from the Nellore Schist Belt, SE India: textural, cathodoluminescence, and SHRIMP U–Pb data. Contributions to Mineralogy and Petrology 162, 867-888.

Wan, Y.S., Dong, C.Y., Xie, H.Q., Wilde, S.A., Liu, S.J., Li, P.C., Ma, M.Z., Li, Y., Wang, Y.Q., Wang, K.L., Liu, D.Y., 2023. Hadean to early Mesoarchean rocks and zircons in the North China Craton: A review. Earth-Science Reviews 243, 104489.

Wang, D., Romer, R.L., Guo, J.-h., Glodny, J., 2020. Li and B isotopic fingerprint of Archean subduction. Geochimica et Cosmochimica Acta 268, 446-466.

Wang, W., Liu, S., Cawood, P.A., Yao, J., Gao, L., Guo, R., Hu, F., Lu, D., He, X., 2024a. Early Neoarchean alternation of plate subduction and deep mantle upwelling. Precambrian Research 402, 107303.

Wang, X., Ge, R.-F., Zheng, Y.-F., Zhu, W.-B., Li, S.-Z., Tian, R.-S., Wang, Y., Rong, Y.-W., 2024b. Successful subduction of oceanic plate after failed attempts in the Late Archean: Petrological and geochemical constraints. Earth and Planetary Science Letters 644, 118944.

Wasserburg, G.J., Jacobsen, S.B., DePaolo, D.J., McCulloch, M.T., Wen, T., 1981. Precise determination of SmNd ratios, Sm and Nd isotopic abundances in standard solutions. Geochimica et Cosmochimica Acta 45, 2311-2323.

Wiedenbeck, M., Alle, P., Corfu, F., Griffin, W.L., Meier, M., Oberli, F.v., Quadt, A.v., Roddick, J., Spiegel, W., 1995. Three natural zircon standards for U-Th-Pb, Lu-Hf, trace element and REE analyses. Geostandards newsletter 19, 1-23.

Wu, F., Ge, W., Sun, D., Lin, Q., Zhou, Y., 1997. The Sm-Nd, Rb-Sr isotopic ages of the Archean granites in southern Jilin province. Acta Petrologica Sinica 13, 499-506.

Wu, K.K., Zhao, G.C., Sun, M., Yin, C.Q., He, Y.H., Tam, P.Y., 2013. Metamorphism of the northern Liaoning Complex: Implications for the tectonic evolution of Neoarchean basement of the Eastern Block, North China Craton. Geoscience Frontiers 4, 305-320.

Wu, M.L., Lin, S.F., Wan, Y.S., Gao, J.F., Stern, R.A., 2021. Episodic Archean crustal accretion in the North China Craton: Insights from integrated zircon U-Pb-Hf-O isotopes of the Southern Jilin Complex, northeast China. Precambrian Research 358, 106150.

Wu, Z., Wang, C., Song, S., Allen, M.B., Kusky, T., Su, L., 2022. Ultrahigh-pressure peridotites record Neoarchean collisional tectonics. Earth and Planetary Science Letters 596, 117787.

Zafar, T., Leng, C.B., Mahar, M.A., Alam, M., Zhang, X.C., Chen, W.T., Rehman, H.U., Rehman, S.U., 2020. Petrogenesis, platinum-group element geochemistry and geodynamic evolution of the Cretaceous Chilas gabbros, Kohistan island arc, NE Pakistan. Lithos 372-373, 105691.

Zhai, M.G., 2011. Cratonization and the Ancient North China Continent: A summary and review. Science China Earth Sciences 54, 1110-1120.

Zhai, M.G., 2014. Multi-stage crustal growth and cratonization of the North China Craton.

Geoscience Frontiers 5, 457-469.

Zhai, M.G., Zhao, L., Zhu, X.Y., Jiao, S.J., Zhou, Y.Y., Zhou, L.G., 2020. Review and overview for the frontier hotspot: Early continents and start of plate tectonics. Acta Petrologica Sinica 36, 2249-2275.

Zhang, W., Hu, Z., Spectroscopy, A., 2020. Estimation of Isotopic Reference Values for Pure Materials and Geological Reference Materials. Atomic Spectroscopy 41, 93-102.

Zhang, Z.C., Kang, J.L., Kusky, T., Santosh, M., Huang, H., Zhang, D.Y., Zhu, J., 2012. Geochronology, geochemistry and petrogenesis of Neoproterozoic basalts from Sugetbrak, northwest Tarim block, China: Implications for the onset of Rodinia supercontinent breakup. Precambrian Research 220-221, 158-176.

Zhao, G.C., Cawood, P.A., 2012. Precambrian geology of China. Precambrian Research 222-223, 13-54.

Zhao, G.C., Cawood, P.A., Li, S.Z., Wilde, S.A., Sun, M., Zhang, J., He, Y.H., Yin, C.Q., 2012. Amalgamation of the North China Craton: Key issues and discussion. Precambrian Research 222-223, 55-76.

Zhao, G.C., Sun, M., Wilde, S.A., Li, S.Z., 2005. Late Archean to Paleoproterozoic evolution of the North China Craton: key issues revisited. Precambrian Research 136, 177-202.

Zhao, L., Guo, F., Fan, W.M., Huang, M.W., 2019. Roles of Subducted Pelagic and Terrigenous Sediments in Early Jurassic Mafic Magmatism in NE China: Constraints on the Architecture of Paleo-Pacific Subduction Zone. Journal of Geophysical Research: Solid Earth 124, 2525-2550.

Zhong, Y., Kusky, T., Wang, L., Polat, A., Liu, X., Peng, Y., Luan, Z., Wang, C., Wang, J., Deng, H., 2021. Alpine-style nappes thrust over ancient North China continental margin demonstrate large Archean horizontal plate motions. Nature Communications 12, 6172.

Zhong, Y., Kusky, T.M., Wang, L., 2022. Giant sheath-folded nappe stack demonstrates extreme subhorizontal shear strain in an Archean orogen. Geology 50, 577-582.

Figure Captions

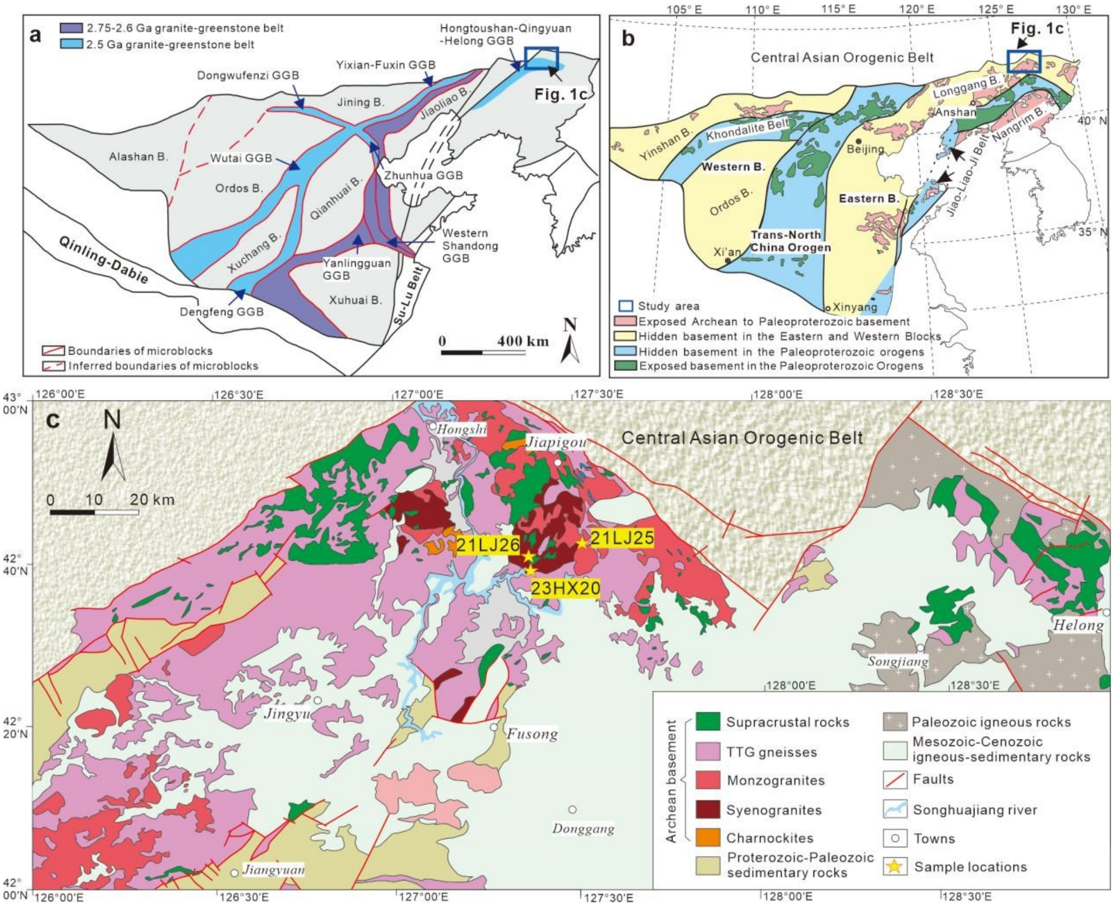

Fig. 1. (a, b) Subdivision of the North China Craton (a after Tang and Santosh, 2018; b after Zhao et al., 2005); (c) Regional geological map of southern Jilin terrane (after Li et al., 2023). Abbreviations: B.-Block; GGB-granite-greenstone belt.

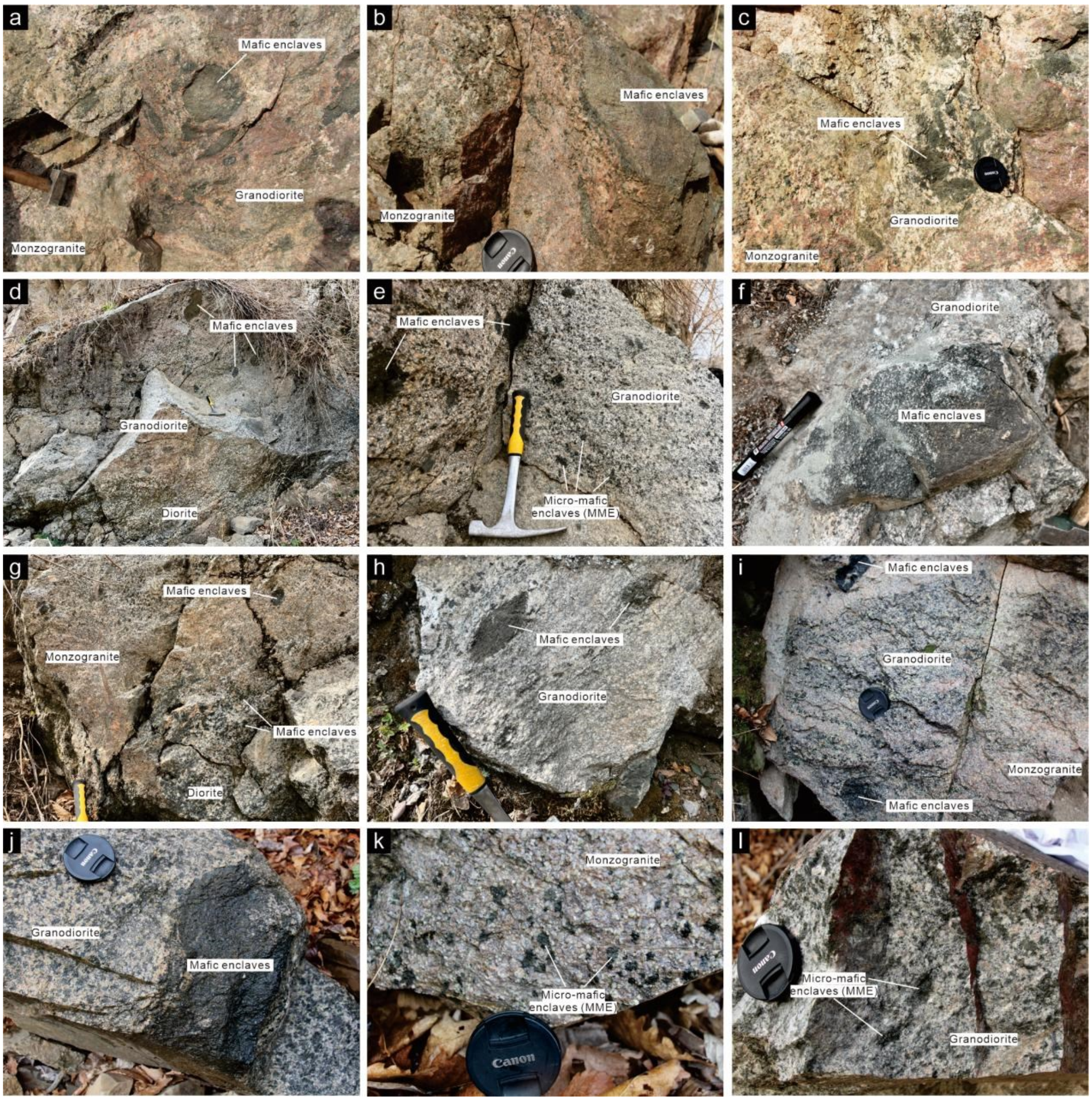

Fig. 2 Photographs of outcrops (a-l) showing the lithological features of different rocks and contact relationships between mafic enclaves and surrounding rocks.

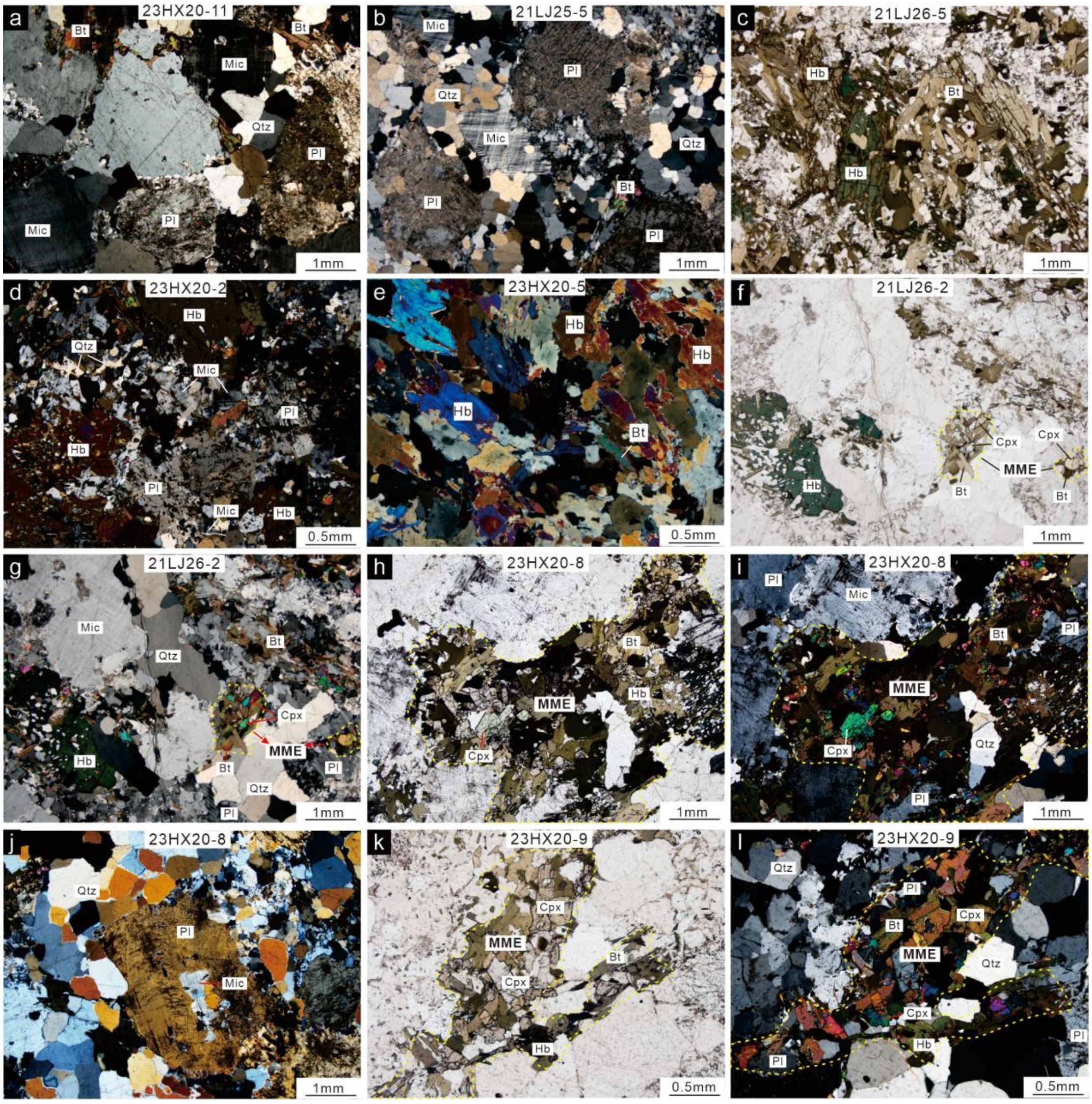

Fig. 3 Photomicrographs of granitoids and mafic enclaves. (a) Syenogranite sample 23HX20-11; (b) Monzogranite sample 21LJ25-5; (c, d) Amphibolite samples 21LJ26-5 and 23HX20-2; (e) Hornblendite sample 23HX20-5; (f, g) Granodiorite sample 21LJ26-2; (h-i) Micro-mafic enclaves (MME) within the granodiorite sample 23HX20-8; (j) Coarse plagioclase grain enclosing microcline core within the granodiorite sample 23HX20-8; (k-l) Micro-mafic enclaves within the quartz diorite sample 23HX20-9. Bt-biotite; Cpx-Clinopyroxene; Hb-hornblende; Mic-microcline; Pl-plagioclase; Qtz-quartz.

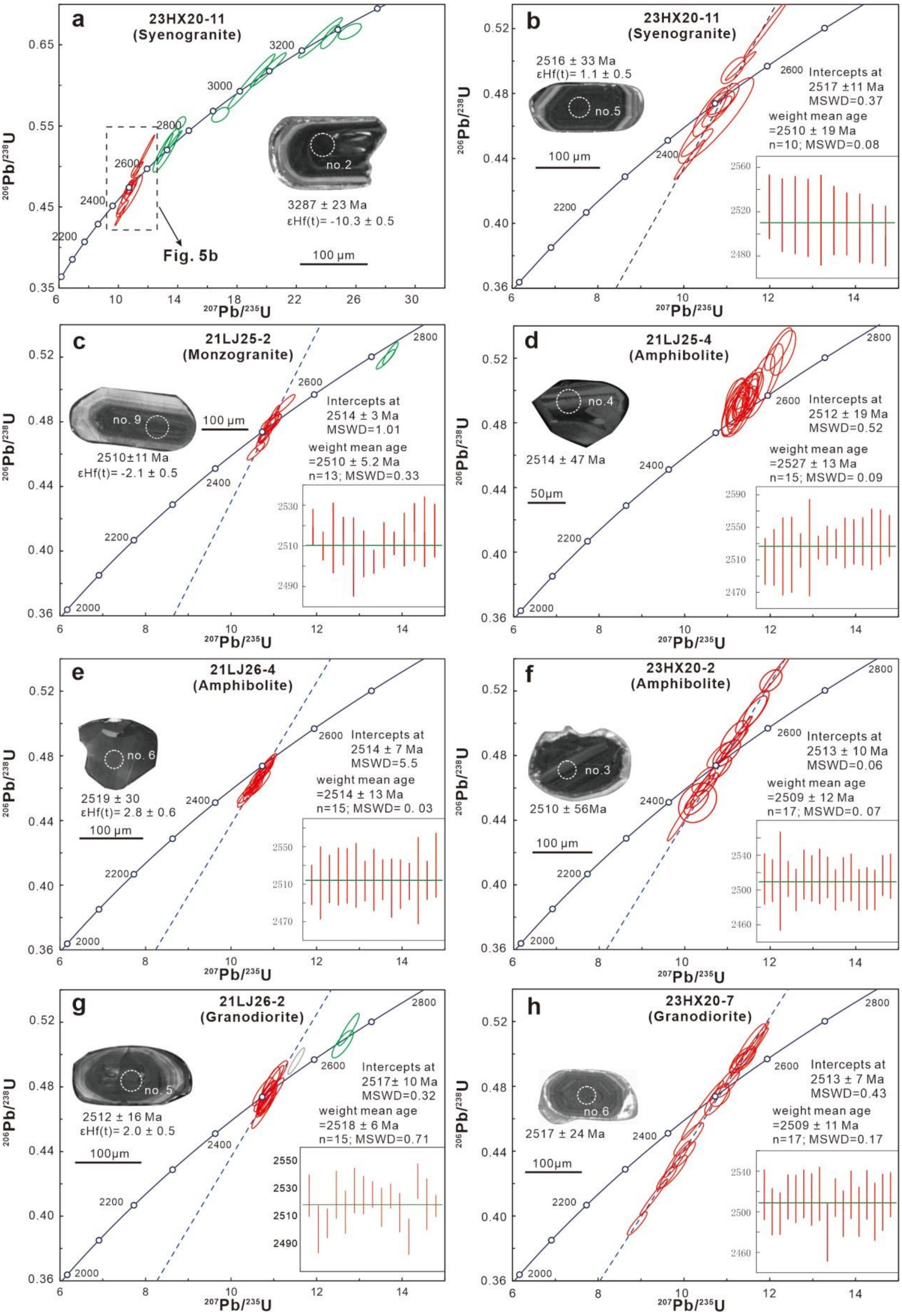

Fig. 4 Concordia diagrams of zircon U–Pb dating and representative zircon CL images.

Red ellipses represent igneous zircons, while green ellipses are inherited zircons.

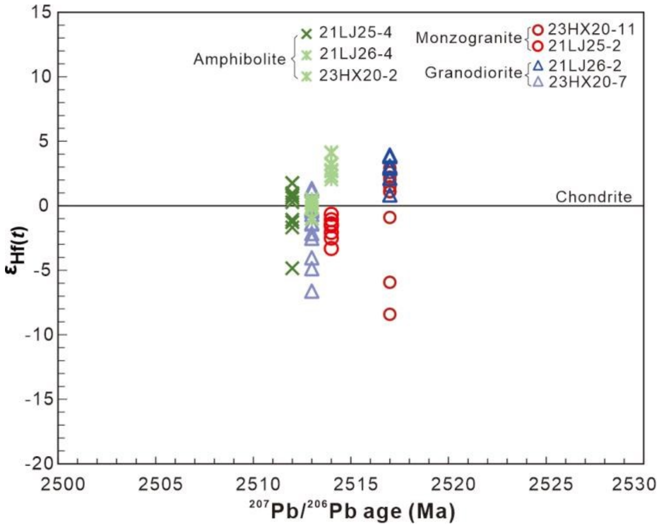

Fig. 5 Diagram of zircon $\varepsilon_{\mathrm{Hf}(t)}$ values versus their ages.

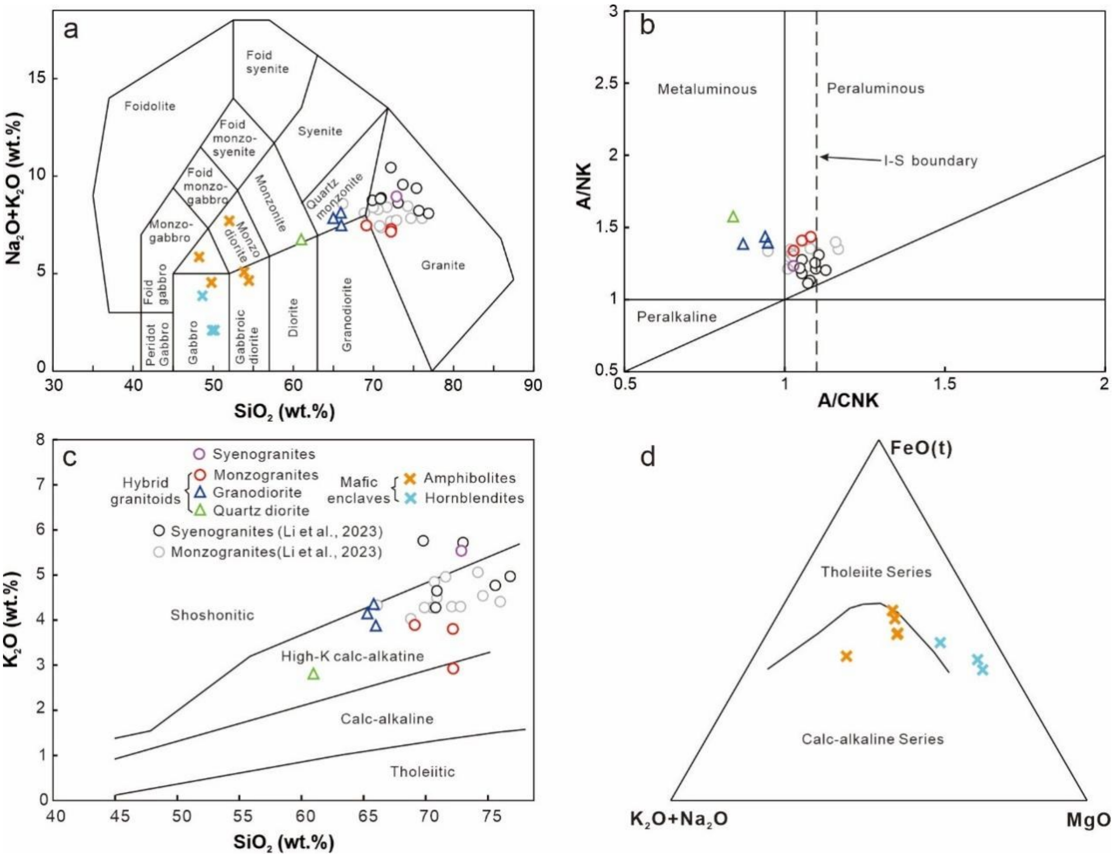

Fig. 6 (a) Total alkali (Na_2O+K_2O)–silica (SiO_2) (TAS) diagram of (Middlemost, 1994); (b) Diagram of A/NK–A/CNK (Maniar and Piccoli, 1989); (c) Diagram of K_2O–SiO_2 (Rickwood, 1989); (d) Ternary diagram of (K_2O + Na_2O)–MgO–FeO(t) (Irvine and Baragar, 1971). Data for potassic granites within the southern Jilin terrane are from Li et al. (2023).

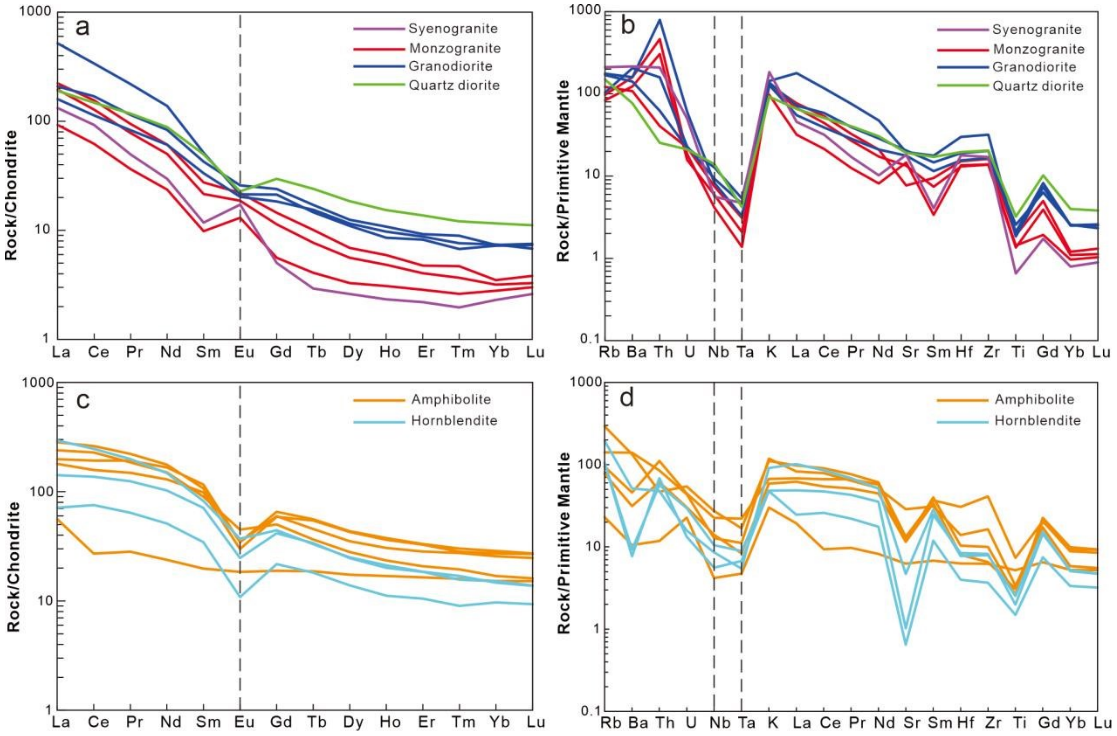

Fig. 7 Diagrams of chondrite-normalized rare earth elements and primitive mantle-normalized trace element for granitoids (a, b) and mafic enclaves (c, d). Normalized chondrite and primitive mantle values are from Sun and McDonough (1989).

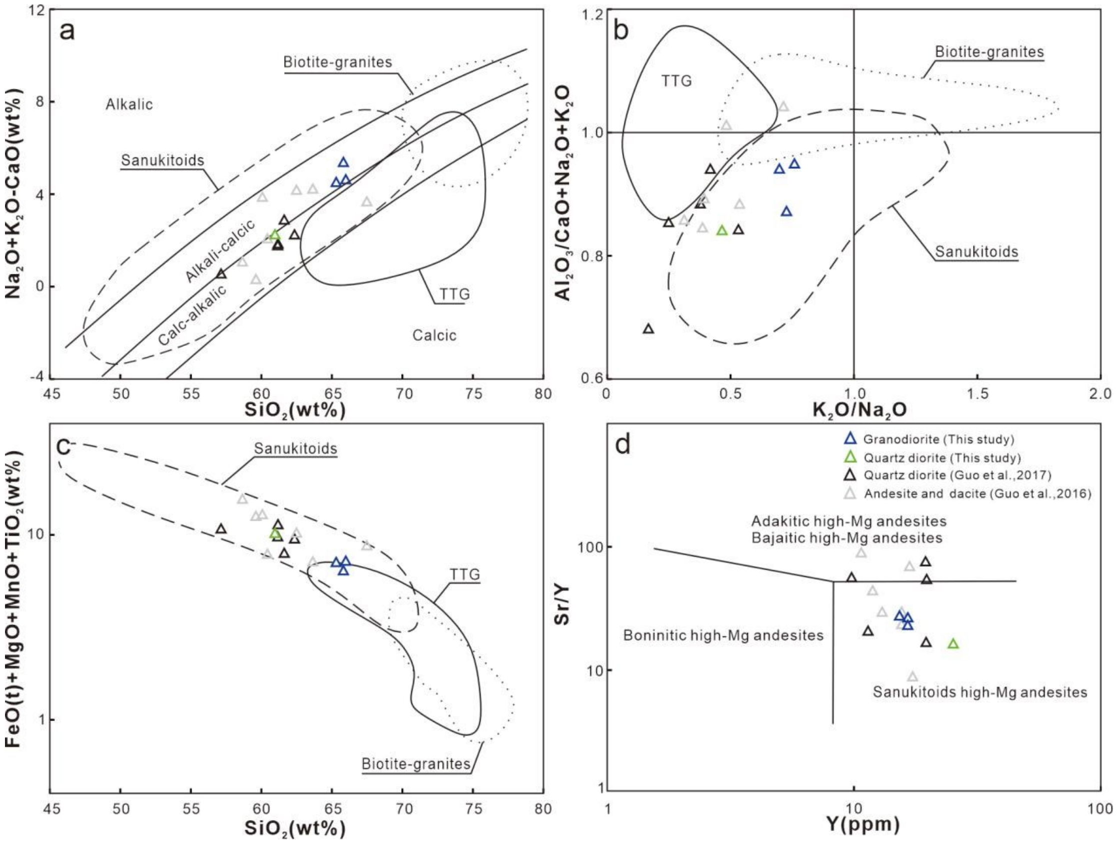

Fig. 8. Discrimination diagrams for sanukitoid. (a) Diagram of (Na_2O+K_2O-CaO)–SiO_2; (b) Diagram of A/CNK–K_2O/Na_2O; (c) Diagram of (FeO(t)+MgO+MnO+TiO_2)–SiO_2 (Laurent et al., 2014); (d) Diagram of (Sr/Y)–Y (Kamei et al., 2004); some reported sanukitoid data are from Guo et al. (2016, 2017).

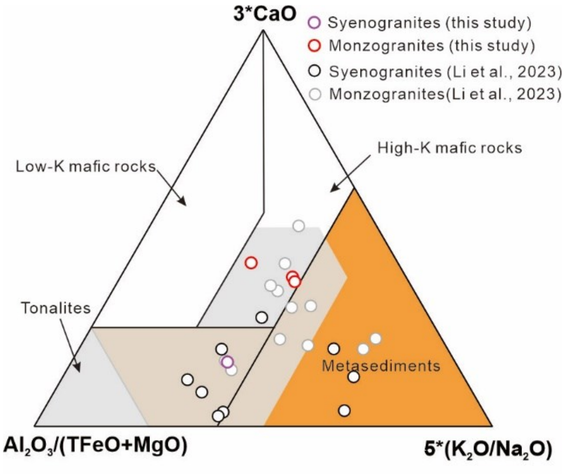

Fig. 9 Ternary diagram of Al_2O_3/(TFeO + MgO)–3*CaO–5*(K_2O/Na_2O) (Laurent et al., 2014; Sun et al., 2025); some reported geochemical data are from Li et al. (2023).

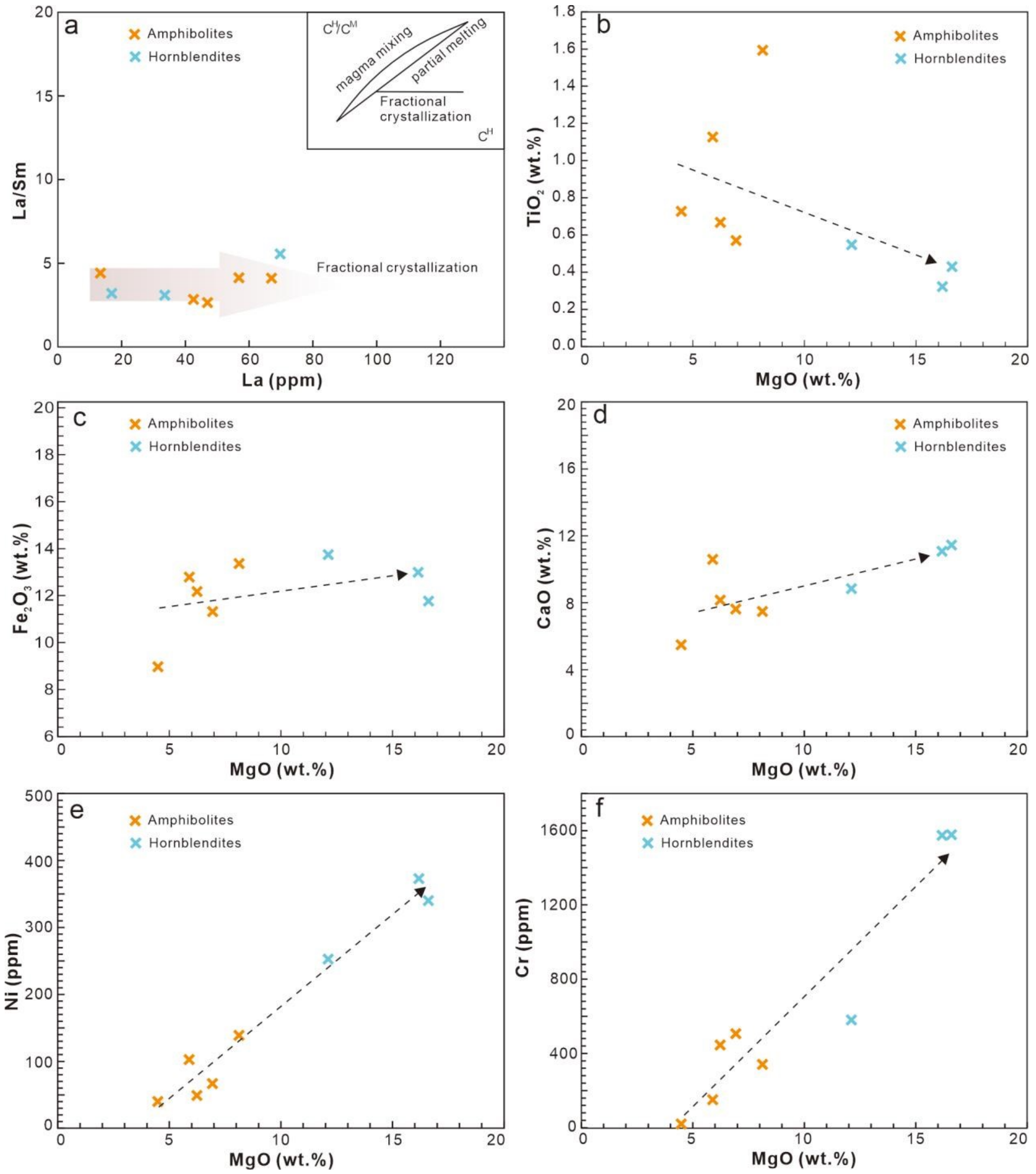

Fig. 10 Geochemical data for amphibolites and hornblendites. (a) Diagram of La/Sm *versus* La showing fractional crystallization trends; (b-f) Plots of selected oxides and trace elements versus MgO.

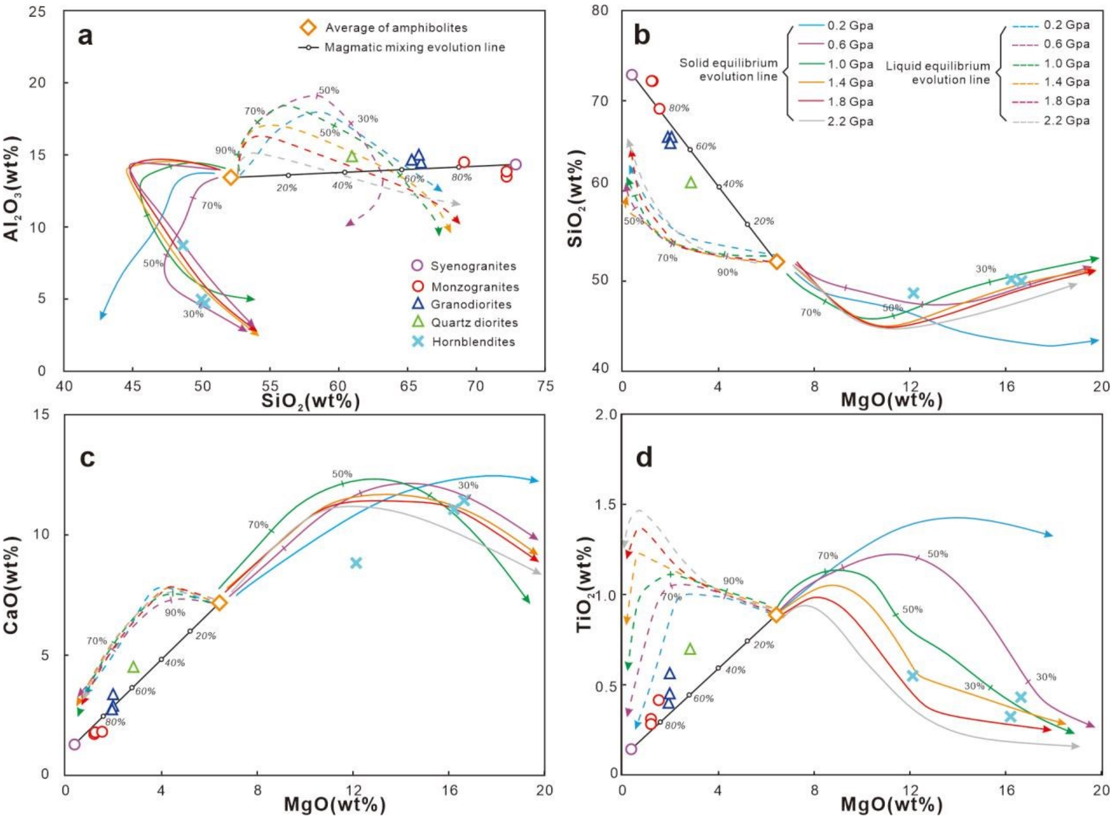

Fig. 11 Modelling diagrams showing the equilibrium crystallization and magma mixing processes using rhyolite-MELTS software (version 1.0.2; Gualda et al., 2012).

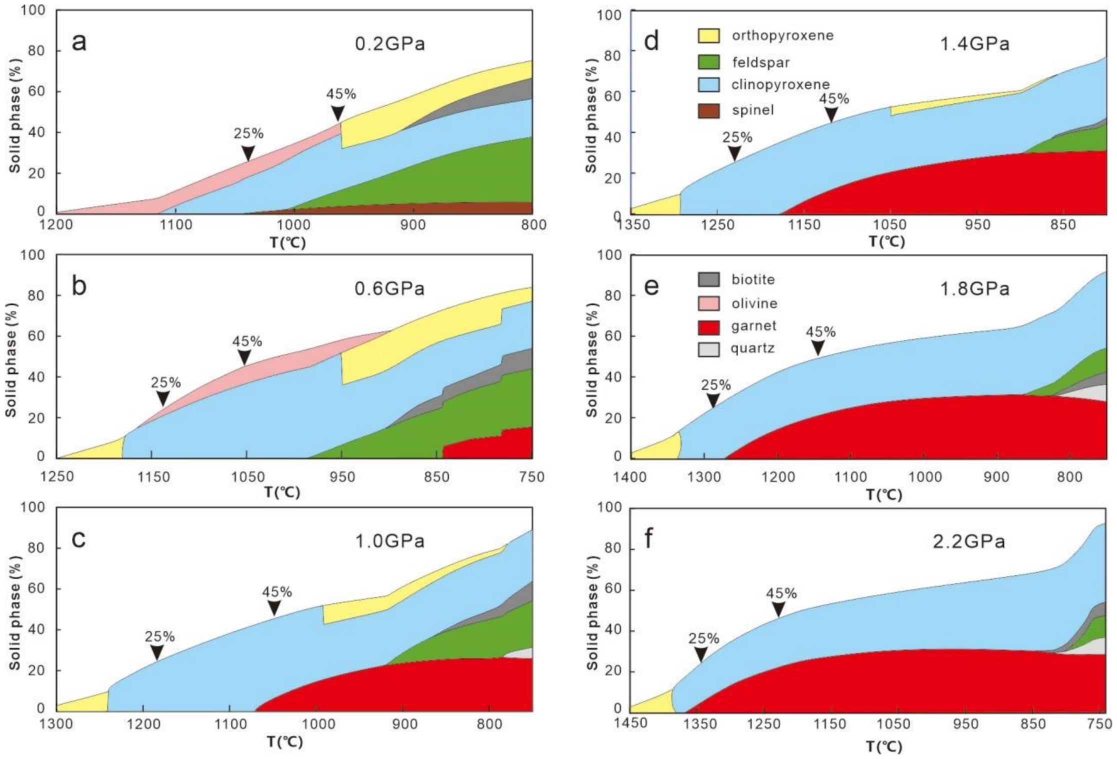

Fig. 12 Results of modelling showing variation in solid phases during isobaric crystallization process under pressures of (a) 0.2, (b) 0.6, (c) 1.0, (d) 1.4, (e) 1.8, and (f) 2.2 GPa. Calculations were performed by rhyolite-MELTS software (version 1.0.2; Gualda et al., 2012).

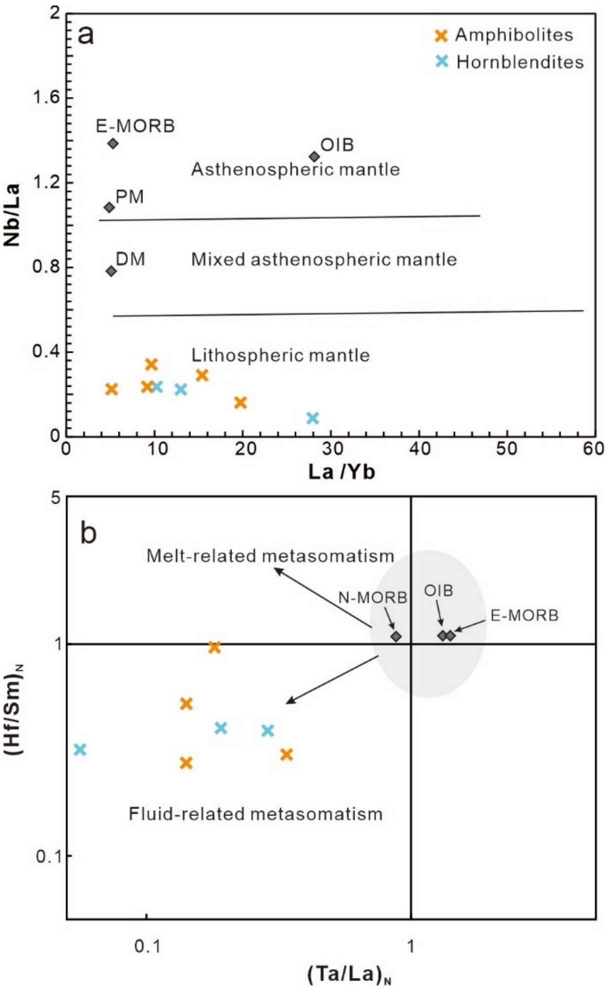

Fig. 13 Geochemical data for amphibolites and hornblendites. (a) (Nb/La)–(La/Yb) diagram (Zafar et al., 2020); (b) (Hf/Sm)$_N$–(Ta/La)$_N$ (La Flèche et al., 1998). Normalized values are from Sun and McDonough (1989).

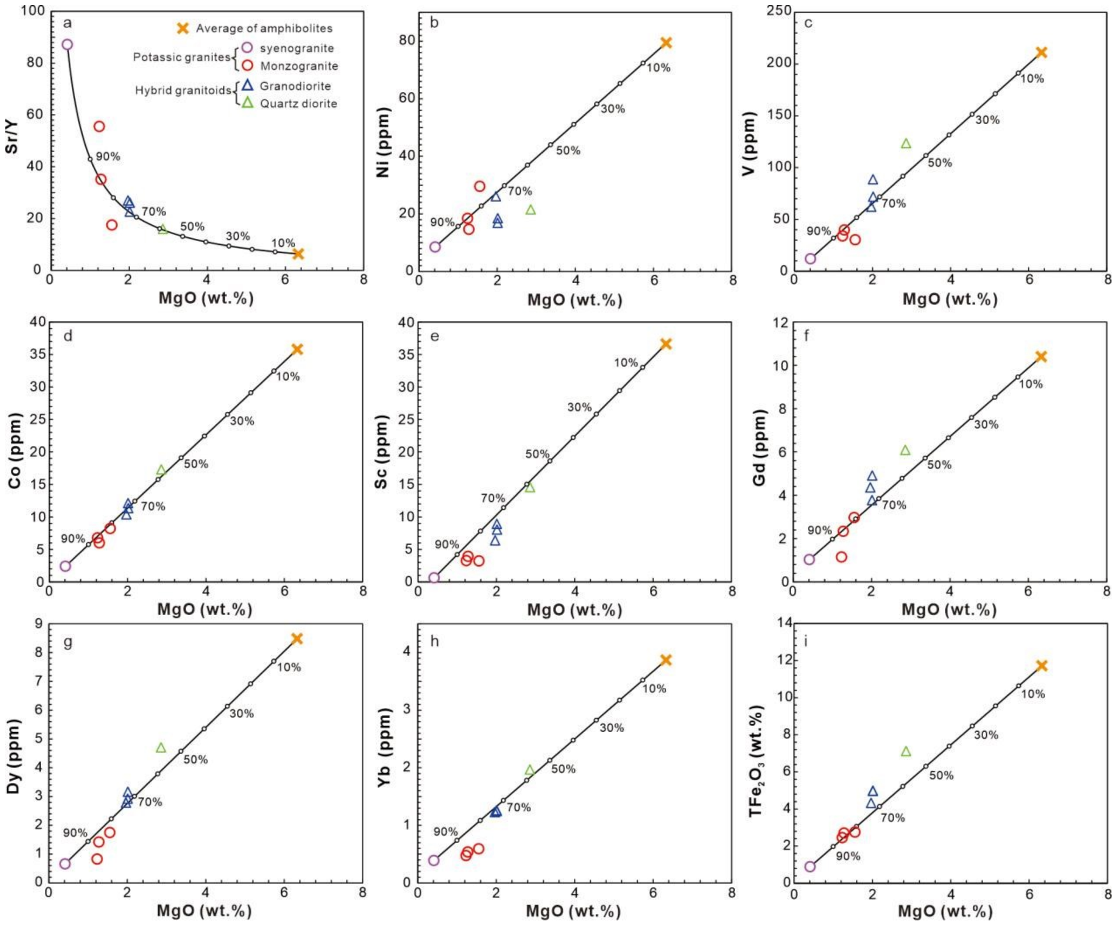

Fig. 14 Magma mixing modelling showing strong, positive, and linear correlation (b-i) between selected major oxides and trace elements with MgO. Measured Sr/Y ratios and MgO contents show a negative correlation (a) defined by a mixing line.

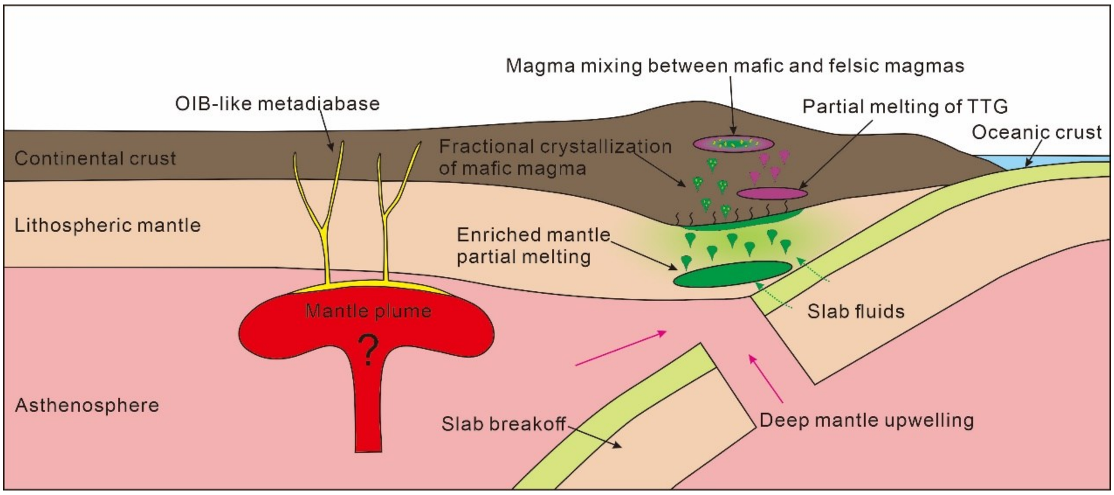

Fig. 15 Schematic cross section of the Jilin terrane of the NCC at 2.5 Ga illustrating the range of geological processes that led to formation of the rock suites described in this work. See main text for discussion. ~~During the late Neoarchean, the magmatic activity in the southern Jilin Terrane was dominated by the amalgamation of microblocks during subduction-accretion processes. This tectonic event was typically accompanied by slab break-off and asthenospheric upwelling, which facilitated partial melting of the enriched mantle and triggered extensive mafic magmatism. These magmas were subsequently underplated beneath the thickened lower crust, triggering the partial melting of pre-existing TTG rocks and the formation of potassic magmas. As the mafic magma ascended, it underwent significant crystallization fractionation before being injected into the contemporaneous potassic magmas. The interaction between the mafic and felsic magmas led to the formation of a granodiorite-diorite series. The late Neoarchean OIB-type mafic dykes within the southern Jilin terrane might suggest the activity of localized mantle plume (Cheng et al., 2024).~~